

CONFORMAL WASSERSTEIN DISTANCE: COMPARING DISK AND SPHERE-TYPE SURFACES IN POLYNOMIAL TIME II, COMPUTATIONAL ASPECTS

Y. LIPMAN, J. PUENTE, I. DAUBECHIES

ABSTRACT. This paper is a companion paper to [19]. We provide numerical procedures and algorithms for computing the alignment of and distance between two disk type surfaces. We furthermore generalize the framework to support sphere-type surfaces, prove a result connecting this distance to geodesic distortion, and provide convergence analysis on the discrete approximation to the arising mass-transportation problems.

1. INTRODUCTION AND BACKGROUND

Alignment of surfaces plays a role in a wide range of scientific disciplines. It is a standard problem in comparing different scans of manufactured objects; various algorithms have been proposed for this purpose in the computer graphics literature. It is often also a crucial step in a variety of problems in medicine and biology; in these cases the surfaces tend to be more complex, and the alignment problem may be harder. For instance, neuroscientists studying brain function through functional Magnetic Resonance Imaging (fMRI) typically observe several people performing identical tasks, obtaining readings for the corresponding activity in the brain cortex of each subject. In a first approximation, the cortex can be viewed as a highly convoluted 2-dimensional surface. Because different cortices are folded in very different ways, a synthesis of the observations from different subjects must be based on appropriate mappings between pairs of brain cortex surfaces, which reduces to a family of surface alignment problems [9, 29]. In another example, paleontologists studying molar teeth of mammals rely on detailed comparisons of the geometrical features of the tooth surfaces to distinguish species or to determine similarities or differences in diet [2].

Mathematically, the problem of surface alignment can be described as follows: given two 2-surfaces \mathcal{M} and \mathcal{N} , find a mapping $f : \mathcal{M} \rightarrow \mathcal{N}$ that preserves, as best possible, “important properties” of the surfaces. The nature of the “important properties” depends on the problem at hand. In this paper, we concentrate on preserving the geometry, i.e., we would like the map f to preserve intrinsic distances, to the extent possible. In terms of the examples listed above, this is the criterion traditionally selected in the computer graphics literature; it also corresponds to the point of view of paleontologists studying tooth surfaces. To align cortical surfaces, one typically uses the Talairach method [18] (which relies on geometrically defined landmarks and is thus geometric in nature as well), although alignment based on functional correspondences has been proposed more recently [29].

In [19] a novel alignment procedure between disk type surfaces, based on uniformization theory and optimal mass transportation, is proposed. In a nutshell, the method maps two surfaces \mathcal{M}, \mathcal{N} to metric densities μ, ν defined on the hyperbolic disk $\mathcal{D} = \{z \mid |z| < 1\}$, their canonical uniformization space. (Apart from simplifying the description of the surface, this also removes any effect of global translations and rotations on the description of each individual surface.) The alignment problem can then be studied in the framework of Kantorovich mass-transportation [16] between these metric densities. Mass-transportation seeks to minimize the “average distance” over which mass needs to be “moved” (in the most efficient such moving procedure) to transform one mass density μ into another, ν :

$$(1.1) \quad T_d(\mu, \nu) = \inf_{\pi \in \Pi(\mu, \nu)} \int_{\mathcal{D} \times \mathcal{D}} d(z, w) d\pi(z, w),$$

where $d(z, w)$ is a cost function, and $\Pi(\mu, \nu)$ is the collection of probability measures on $\mathcal{D} \times \mathcal{D}$ with marginals μ and ν (resp.), that is, for $A \subset \mathcal{D}$, $B \subset \mathcal{D}$, $\pi(A \times \mathcal{D}) = \mu(A)$ and $\pi(\mathcal{D} \times B) = \nu(B)$.

In our case the uniformizing metric density (or conformal factor) corresponding to an initial surface is not unique, but is defined only up to a Möbius transformation. Because a naïve application of mass-transportation on the hyperbolic disk would not possess the requisite invariance under Möbius transformations, we generalize the mass-transportation framework, and replace the metric $d(x, y)$ traditionally used in defining the “average displacement distance” by a metric that depends on μ and ν , $d_{\mu, \nu}^R(z, w)$, measuring the dissimilarity between the two metric densities on neighborhoods of x and y :

$$(1.2) \quad T_d^R(\mu, \nu) = \inf_{\pi \in \Pi(\mu, \nu)} \int_{\mathcal{D} \times \mathcal{D}} d_{\mu, \nu}^R(z, w) d\pi(z, w).$$

Introducing neighborhoods (through the parameter R) also makes the definition less sensitive to noise in practical applications. The optimal way of transporting mass in this generalized framework, in which the orientation in space of the original surfaces is “factored away”, automatically defines a corresponding optimal way of aligning the surfaces.

This approach also allows us to define a new distance between surfaces. The average distance over which mass needs transporting (to transform one metric density into the other) quantifies the extent to which the two surfaces differ. Furthermore, this new metric is computable in polynomial time. In this paper, we present and discuss the numerical algorithm that achieves this computational goal; furthermore, we indicate how the above ideas can be generalized to other types of surfaces. In particular we show how the distance can be defined for genus zero, or sphere-type, surfaces. We also present a theoretical result directly connecting this distance to the notion of geodesic distortion. Lastly, in order to validate the usefulness of our method, we tested it on various benchmark data sets and compared it to state-of-the-art method.

1.1. Uniformization. Uniformization theory for Riemann surfaces [31, 14] allows conformally flattening disk type surfaces onto the unit disk $\phi : \mathcal{M} \rightarrow \mathcal{D}$, where ϕ is the conformal flattening map, $\mathcal{D} = \{z \mid |z| < 1\}$ is the unit disk, and the disk coordinate system is denoted by $z = x^1 + ix^2$. The surface’s Riemannian metric g is then pushed-forward to a diagonal metric tensor

$$\tilde{g} = \phi_*g = \tilde{\mu}(z) \delta_{ij} dx^i \otimes dx^j,$$

where $\tilde{\mu}(z) > 0$, Einstein summation convention is used, and the subscript $*$ denotes the “push-forward” action. The function $\tilde{\mu}$ can also be viewed as the *density function* of the measure $\text{vol}_{\mathcal{M}}$ induced by the Riemann volume element:

$$(1.3) \quad \text{vol}_{\mathcal{M}}(A) = \int_{\phi(A)} \tilde{\mu}(z) dx^1 \wedge dx^2,$$

for (measurable) $A \subset \mathcal{M}$. For a second surface \mathcal{N} with Riemannian metric h we will denote its pushed-forward metric on the uniformization disk \mathcal{D} by $\tilde{h} = \phi_*h = \tilde{\nu}(w) \delta_{ij} dy^i \otimes dy^j$, where the coordinates in the unit disk are $w = y^1 + iy^2$.

We use the hyperbolic metric on the unit disk $(1 - |z|^2)^{-2} \delta_{ij} dx^i \otimes dx^j$ as a reference metric, and the surface density w.r.t the hyperbolic metric (conformal scaling) is

$$(1.4) \quad \mu^H(z) := (1 - |z|^2)^2 \tilde{\mu}(z),$$

where the superscript H stands for hyperbolic. We shall often drop this superscript: unless otherwise stated $\mu = \mu^H$, and $\nu = \nu^H$ in what follows. The density function $\mu = \mu^H$ satisfies

$$\text{vol}_{\mathcal{M}}(A) = \int_{\phi(A)} \mu(z) d\text{vol}_H(z),$$

where $d\text{vol}_H(z) = (1 - |z|^2)^{-2} dx^1 \wedge dx^2$.

The conformal mappings of \mathcal{D} to itself are the disk-preserving Möbius transformations $m \in M_D$, a family with three real parameters, which is the group of isometries of the hyperbolic disk:

$$(1.5) \quad m(z) = e^{i\theta} \frac{z - a}{1 - \bar{a}z}, \quad a \in \mathcal{D}, \theta \in [0, 2\pi).$$

The pull-back $m^*\mu(z)$ and the push-forward $m_*\mu(w)$ of the density μ by the Möbius transformation m are given by the formulas

$$(1.6) \quad m^*\mu(z) = \mu(m(z)),$$

and

$$(1.7) \quad m_*\mu(w) = \mu(m^{-1}(w)),$$

respectively.

It follows that checking whether or not two surfaces \mathcal{M} and \mathcal{N} are isometric, or searching for (near-) isometries between \mathcal{M} and \mathcal{N} , is greatly simplified by considering the conformal mappings from \mathcal{M}, \mathcal{N} to \mathcal{D} : once the (hyperbolic) density functions μ and ν are known, it suffices to identify $m \in M_D$ such that $\nu(m(z))$ equals $\mu(z)$ (or “nearly” equals, in a sense to be made precise).

1.2. Optimal volume transportation for surfaces. The only component we need to introduce for adapting optimal transportation to align surfaces is the Möbius invariant cost function $d_{\mu,\nu}^R(z, w)$ that is plugged into the transportation framework (1.1). This special cost function $d_{\mu,\nu}^R(z, w)$ indicates the extent to which a neighborhood of the point z in (\mathcal{D}, μ) , the (conformal representation of the) first surface, is isometric with a neighborhood of the point w in (\mathcal{D}, ν) , the (conformal representation of the) second surface. Two definitions are in order: the neighborhoods we will use, and how we shall characterize the (dis)similarity of two neighborhoods, equipped with different metrics.

For the neighborhoods, we take the geodesic disks $\Omega_{z_0,R}$, of the hyperbolic disk, where we let z_0 range over the disk, but keep the radius $R > 0$ fixed. The following gives an easy procedure to construct these disks. If $z_0 = 0$, then the hyperbolic geodesic disks centered at $z_0 = 0$ are also “standard” (i.e. Euclidean) disks centered at 0: $\Omega_{0,R} = \{z; |z| \leq r_R\}$, where $r_R = \operatorname{arctanh}(r) = R$. The hyperbolic disks around other centers are images of these central disks under Möbius transformations (= hyperbolic isometries): setting $m(z) = (z - z_0)(1 - z\bar{z}_0)^{-1}$, we have

$$(1.8) \quad \Omega_{z_0,R} = m^{-1}(\Omega_{0,R}).$$

Next, the (dis)similarity of the pairs $(\Omega_{z_0,R}, \mu)$ and $(\Omega_{w_0,R}, \nu)$ is defined via pull-back of ν and using the standard induced norm on the space of 2-covariant tensors. The final cost function is achieved by taking the infimum over all Möbius transformations m such that $m(z) = w$:

$$(1.9) \quad d_{\mu,\nu}^R(z_0, w_0) := \inf_{m \in M_D, m(z_0) = w_0} \int_{\Omega_{z_0,R}} |\mu(z) - (m^*\nu)(z)| d\operatorname{vol}_H(z),$$

where $d\operatorname{vol}_H(z) = (1 - |z|^2)^{-2} dx \wedge dy$ is the volume form for the hyperbolic disk.

As proved in [19] $d_{\mu,\nu}^R(\cdot, \cdot)$ satisfies metric properties and as a consequence $\mathbf{d}^R(\mathcal{M}, \mathcal{N}) = T_d^R(\mu, \nu)$ defines a semi-metric in the space of disk-type surfaces. To ensure that this is a metric rather than only a semi-metric, we add an extra assumption, namely that no (orientation-preserving) self-isometries exist within each of the compared surfaces. For discussion and more detail we refer the reader to [19].

1.3. Related work. The approach taken in this paper is related to the computer graphics constructions in [21], which rely on the representation of isometries between topologically equivalent simply-connected surfaces by Möbius transformations between their uniformization spaces, and which exploit that 1) the Möbius group has small dimensionality (e.g. 3 for disk-type surfaces and 6 for sphere-type) and 2) changing the metric in one piece of a surface has little influence on the uniformization of distant parts. These two

observations lead, in [21], to fast and particularly effective algorithms to identify near-isometries between differently deformed versions of a surface. In our present context, these same observations lead to a simple algorithm for surface alignment, reducing it to a linear programming problem.

Other distances between surfaces have been used recently for several applications [22]. A prominent mathematical approach to define distances between surfaces considers the surfaces as special cases of *metric spaces*, and uses then the Gromov-Hausdorff (GH) distance between metric spaces [11]. The GH distance between metric spaces X and Y is defined through examining all the isometric embedding of X and Y into (other) metric spaces; although this distance possesses many attractive mathematical properties, it is inherently hard computationally [23, 1]. For instance, computing the GH distance is equivalent to a non-convex quadratic programming problem; solving this directly for correspondences is equivalent to integer quadratic assignment, and is thus NP-hard [6]. In addition, the non-convexity implies that the solution found in practice may be a local instead of a global minimum, and is therefore not guaranteed to give the correct answer for the GH distance. The distance metric between surfaces that we define in this paper does not have these shortcomings because the computation of the distance between surfaces in our approach can be recast as a linear program, and can therefore be implemented using efficient polynomial algorithms that are moreover guaranteed to converge to the correct solution.

It should be noted that in [22], Memoli generalizes the GH distance of [23] by introducing a quadratic mass transportation scheme to be applied to metric spaces already equipped with a measure (mm spaces); he notes that the computation of this Gromov-Wasserstein distance for mm spaces is somewhat easier and more stable to implement than the original GH distance. In our approach we do not need to equip the surfaces we compare with a measure: after uniformization reduces the problem to comparing two disks, we naturally "inherit" two corresponding conformal factors that we interpret as measure densities, for which we then apply an approach similar to the one proposed in [22]. Another crucial aspect in which our work differs from [22] is that, in contrast to the (continuous) quadratic programming method proposed in [22] to compute the Gromov-Wasserstein distance between mm spaces, our conformal approach leads to a convex (even linear) problem, solvable via a linear programming method.

It is worth mentioning that optimal mass transportation has been used in the engineering literature to define interesting metrics between images; in this context the metric is often called the Wasserstein distance. The seminal work for this image analysis approach is the paper by Rubner et al. [28], in which images are viewed as discrete measures, and the distance is called appropriately the "Earth Mover's Distance".

Another related method is presented in the papers of Zeng et al. [33, 34], which also use the uniformization space to match surfaces. Our work differs from that of Zeng et al. in that they use prescribed feature points (defined either by the user or by extra texture information) to calculate an interpolating harmonic map between the uniformization spaces, and then define the final correspondence as a composition of the uniformization maps and this harmonic interpolant. This procedure is highly dependent on the prescribed feature points, provided as extra data or obtained from non-geometric information. In contrast, our work does not use any prescribed feature points or external data, and makes use of only the geometry of the surface; in particular we utilize the conformal structure itself to define deviation from (local) isometry.

Our paper is organized as follows: Section 2 presents the main steps for the discretization of the continuous case and provides algorithmic aspects for the alignment procedure. Section 3 generalizes the method to sphere-type surfaces. Section 4 provides a theoretical result connecting our distance directly to geodesic distortion. Section 5 presents experimental validation of the algorithms and concludes.

2. DISCRETIZATION AND IMPLEMENTATION

Transforming the theoretical framework discussed above into an algorithm requires discretizing the relevant continuous objects. Our general plan is to recast the transportation eq. (1.2) as a linear programming problem between discrete measures. This requires two approximation steps:

1) approximating the surface's uniformization, and

2) discretizing the resulting continuous measures and finding the optimal transport between the discrete measures.

To show how we do this, we first review a few basic notions such as the representation of (approximations to) surfaces by faceted, piecewise flat approximations, called *meshes*, and discrete conformal mappings; the conventions we describe here are the same as adopted in [21].

2.1. Meshes, mid-edge meshes, and discrete conformal mapping. Triangular (piecewise-linear) meshes are a popular choice for the definition of discrete versions of smooth surfaces. We shall denote a triangular mesh by the triple $M = (V, E, F)$, where $V = \{v_i\}_{i=1}^m \subset \mathbb{R}^3$ is the set of vertices, $E = \{e_{i,j}\}$ the set of edges, and $F = \{f_{i,j,k}\}$ the set of faces (oriented $i \rightarrow j \rightarrow k$). When dealing with a second surface, we shall denote its mesh by N . We assume our mesh is homeomorphic to a disk.

Next, we introduce “conformal mappings” of a mesh to the unit disk. Natural candidates for discrete conformal mappings are not immediately obvious. Since we are dealing with piecewise linear surfaces, it might seem natural to select a continuous linear map that is piecewise affine, such that its restriction to each triangle is a similarity transformation. A priori, a similarity map from a triangular face to the disk has 4 degrees of freedom; requiring that the image of each edge remain a shared part of the boundary of the images of the faces abutting the edge, and that the map be continuous when crossing this boundary, imposes 4 constraints for each edge. This quick back of the envelope calculation thus allows $4|F|$ degrees of freedom for such a construction, with $4|E|$ constraints. Since $3|F|/2 \approx |E|$ this problem is over-constrained, and a construction along these lines is not possible. A different approach uses the notion of discrete harmonic and discrete conjugate harmonic functions due to Pinkall and Polthier [25, 27] to define a discrete conformal mapping on the mid-edge mesh (to be defined shortly). This relaxes the problem to define a map via a similarity on each triangle that is continuous through only *one* point in each edge, namely the mid point. We summarize here this procedure, which was also used in [21]; for additional implementation details we refer the interested reader (or programmer) to that paper, which includes a pseudo-code.

The mid-edge mesh $\mathbf{M} = (\mathbf{V}, \mathbf{E}, \mathbf{F})$ of a given mesh $M = (V, E, F)$ is defined as follows. For the vertices $\mathbf{v}_r \in \mathbf{V}$, we pick the mid-points of the edges of the mesh M ; we call these the mid-edge points of M . There is thus a $\mathbf{v}_r \in \mathbf{V}$ corresponding to each edge $e_{i,j} \in E$. If \mathbf{v}_s and \mathbf{v}_r are the mid-points of edges in E that share a vertex in M , then there is an edge $\mathbf{e}_{s,r} \in \mathbf{E}$ that connects them. It follows that for each face $f_{i,j,k} \in F$ we can define a corresponding face $\mathbf{f}_{r,s,t} \in \mathbf{F}$, the vertices of which are the mid-edge points of (the edges of) $f_{i,j,k}$; this face has the same orientation as $f_{i,j,k}$. Note that the mid-edge mesh is not a manifold mesh, as illustrated by the mid-edge mesh in Figure 1, shown together with its “parent” mesh: in \mathbf{M} each edge “belongs” to only one face \mathbf{F} , as opposed to a manifold mesh, in which most edges (the edges on the boundary are exceptions) function as a hinge between two faces. This “lace” structure makes a mid-edge mesh more flexible: it turns out that it is possible to define a piecewise linear map that makes each face in \mathbf{F} undergo a pure scaling (i.e. all its edges are shrunk or extended by the same factor) and that simultaneously flattens the whole mid-edge mesh. By extending this back to the original mesh, we thus obtain a map from each triangular face to a similar triangle in the plane; these individual similarities can be “knitted together” through the mid-edge points, which continue to coincide (unlike most of the vertices of the original triangles).

To determine the flattening map, we use the framework of discrete harmonic and conjugate harmonic functions, first defined and studied by Pinkall and Polthier [25, 27] in the context of discrete minimal surfaces. This framework was first adapted to the present context in [21]; this adaptation is explained in some detail in Appendix B. The flattening map is well-defined at the mid-edges \mathbf{v}_s . As shown in [21] (see also Appendix B) the boundary of the mesh gets mapped onto a region with a straight horizontal slit (see Figure 2, where the boundary points are marked in red). We can assume, without loss of generality, that this slit coincides with the interval $[-2, 2] \subset \mathbb{C}$, since it would suffice to shift and scale the whole figure to make this happen. The holomorphic map $z = w + \frac{1}{w}$ maps the unit disk conformally to $\mathbb{C} \setminus [-2, 2]$, with the boundary of the disk mapped to the slit at $[-2, 2]$; when the inverse of this map is applied to our flattened mid-edge mesh, its image will thus be a mid-edge mesh in the unit disk, with the boundary of the disk corresponding to the boundary of our (disk-like) surface. (See Figure 2.) We shall denote by $\Phi : \mathbf{V} \rightarrow \mathbb{C}$ the concatenation of

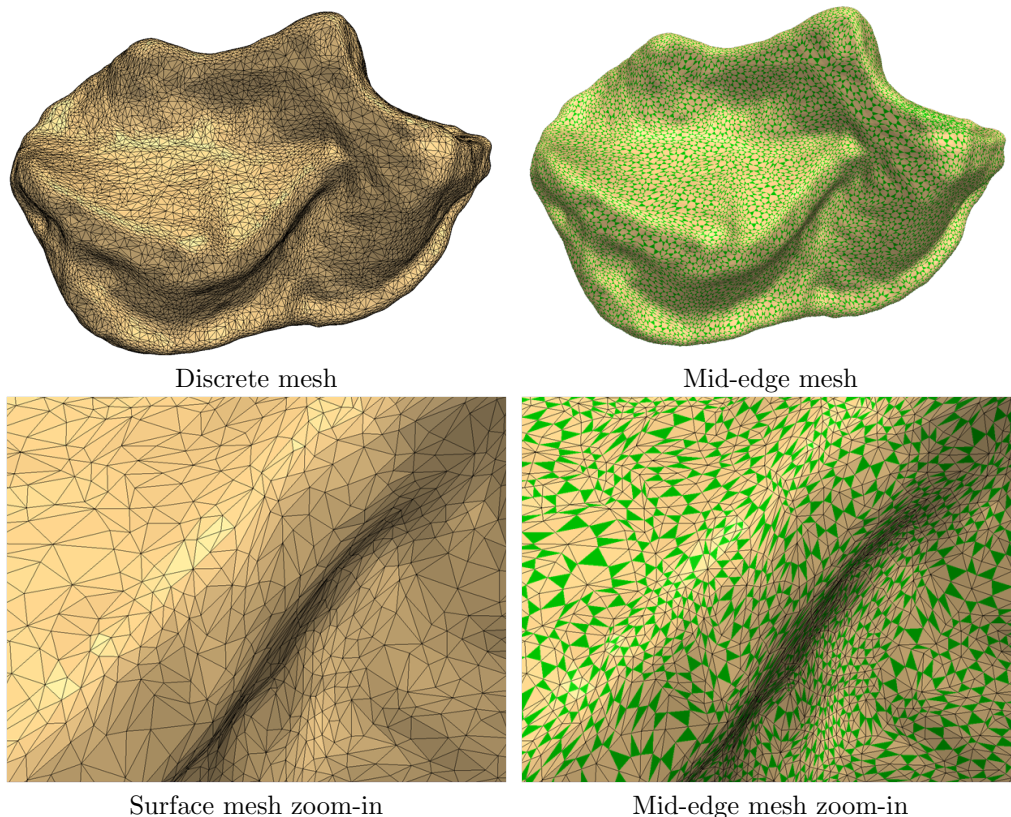


FIGURE 1. A mammalian tooth surface mesh, with the corresponding mid-edge mesh. In the mid-edge mesh, the faces are the smaller green triangles within the faces of the surface mesh.

these different conformal and discrete-conformal maps, from the original mid-edge mesh to the corresponding mid-edge mesh in the unit disk.

Next, we define the Euclidean discrete conformal factors, defined as the density, w.r.t. the Euclidean metric, of the mid-edge triangles (faces), i.e.

$$\mu_{\mathbf{f}_{r,s,t}}^E = \frac{\text{vol}_{\mathbb{R}^3}(\mathbf{f}_{r,s,t})}{\text{vol}(\Phi(\mathbf{f}_{r,s,t}))}.$$

Note that according to this definition, we have

$$\int_{\Phi(\mathbf{f}_{r,s,t})} \mu_{\mathbf{f}_{r,s,t}}^E d\text{vol}_E = \frac{\text{vol}_{\mathbb{R}^3}(\mathbf{f}_{r,s,t})}{\text{vol}_E(\Phi(\mathbf{f}_{r,s,t}))} \text{vol}_E(\Phi(\mathbf{f}_{r,s,t})) = \text{vol}_{\mathbb{R}^3}(\mathbf{f}_{r,s,t}),$$

where vol_E denotes the standard Euclidean volume element $dx^1 \wedge dx^2$ in \mathbb{C} , and $\text{vol}_{\mathbb{R}^3}(\mathbf{f})$ stands for the area of \mathbf{f} as induced by the standard Euclidean volume element in \mathbb{R}^3 . The discrete Euclidean conformal factor at a mid-edge vertex \mathbf{v}_r is then defined as the average of the conformal factors for the two faces $\mathbf{f}_{r,s,t}$ and $\mathbf{f}_{r,s',t'}$ that touch in \mathbf{v}_r , i.e.

$$\mu_{\mathbf{v}_r}^E = \frac{1}{2} \left(\mu_{\mathbf{f}_{r,s,t}}^E + \mu_{\mathbf{f}_{r,s',t'}}^E \right).$$

Figure 2 illustrates the values of the Euclidean conformal factor for the mammalian tooth surface of earlier figures. The discrete hyperbolic conformal factors are defined according to the following equation, consistent with the convention adopted in section 1,

$$(2.1) \quad \mu_{\mathbf{v}_r}^H = \mu_{\mathbf{v}_r}^E (1 - |\Phi(\mathbf{v}_r)|^2)^2.$$

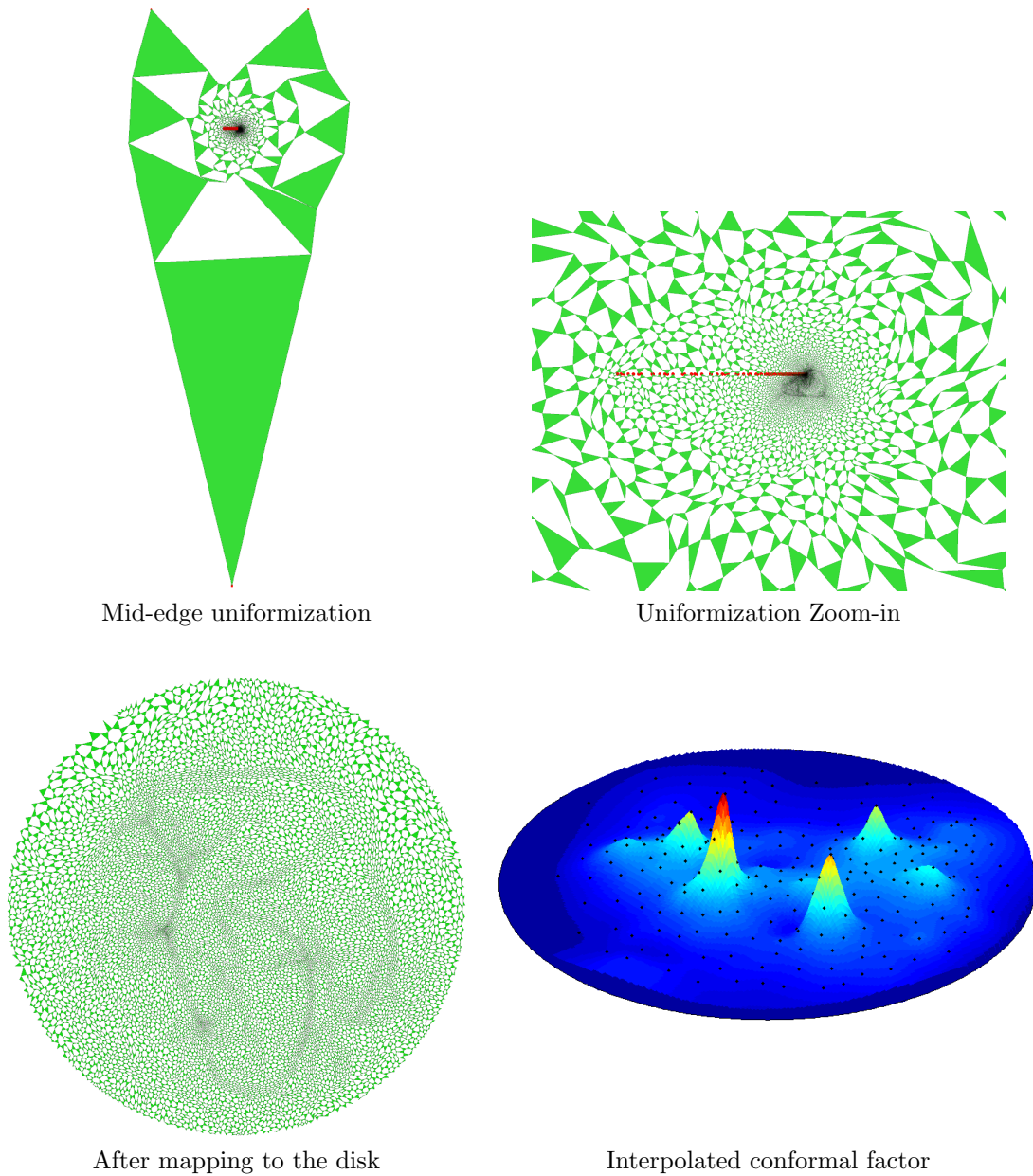


FIGURE 2. The discrete conformal transform to the unit disk for the surface of Figure 1, and the interpolation of the corresponding discrete conformal factors (plotted with the JET color map in Matlab). The red points in the top row’s images show the boundary points of the surface.

As before, we shall often drop the superscript H : unless otherwise stated, $\mu = \mu^H$, and $\nu = \nu^H$.

The (approximately) conformal mapping of the original mesh to the disk is completed by constructing a smooth interpolant $\Gamma_\mu : \mathcal{D} \rightarrow \mathbb{R}$, that interpolates the discrete conformal factor so far defined only at the vertices in $\Phi(\mathbf{V})$; Γ_ν is constructed in the same way. In practice we use Thin-Plate Splines, i.e. functions of the type

$$\Gamma_\mu(z) = p_1(z) + \sum_i b_i \psi(|z - z_i|),$$

where $\psi(r) = r^2 \log(r^2)$, $p_1(z)$ is a linear polynomial in x^1, x^2 , and $b_i \in \mathbb{C}$; p_1 and the b_i are determined by the data that need to be interpolated. Similarly $\Gamma_\nu(w) = q_1(w) + \sum_j c_j \psi(|w - w_j|)$ for some constants $c_j \in \mathbb{C}$ and a linear polynomial $q_1(w)$ in y^1, y^2 . We use as interpolation centers two point sets $Z = \{z_i\}_{i=1}^n$, and $W = \{w_j\}_{j=1}^p$ defined in the next subsection for the discretization of the measures. The bottom-right part of Figure 2 shows the result of this interpolation procedure for the data given by the black dots.

We also note that for practical purposes it is sometimes advantageous to use Smoothing Thin-Plate Splines:

$$\Gamma_\mu(z) = \operatorname{argmin}_\gamma \left\{ \lambda \sum_r |\mu_{\mathbf{v}_r} - \gamma(\Phi(\mathbf{v}_r))|^2 + (1 - \lambda) \int_{\mathcal{D}} \left(\frac{\partial^2 \gamma}{\partial(x^1)^2} \right)^2 + \left(\frac{\partial^2 \gamma}{\partial x^1 \partial x^2} \right)^2 + \left(\frac{\partial^2 \gamma}{\partial(x^2)^2} \right)^2 dx^1 \wedge dx^2 \right\}.$$

when using these, we picked the value 0.99 for the smoothing factor λ .

2.2. Discretizing continuous measures and their transport. In this subsection we indicate how to construct discrete approximations $T_{\text{discr.,}d}^R(\xi, \zeta)$ for the distance $\mathbf{d}^R(\mathcal{X}, \mathcal{Y}) = T_d^R(\xi, \zeta)$ between two surfaces \mathcal{X} and \mathcal{Y} , each characterized by a corresponding smooth density on the unit disk \mathcal{D} (ξ for \mathcal{X} , ζ for \mathcal{Y}). (In practice, we will use the smooth functions Γ_μ and Γ_ν for ξ and ζ .) We shall use discrete optimal transport to construct our approximation $T_{\text{discr.,}d}^R(\xi, \zeta)$, based on sampling sets for the surfaces, with convergence to the continuous distance as the sampling is refined.

To quantify how fine a sampling set Z is, we use the notion of *fill distance* $\varphi(Z)$:

$$\varphi(Z) := \sup \{ r > 0 \mid z \in \mathcal{M} : B_g(z, r) \cap Z = \emptyset \},$$

where $B_g(z, r)$ is the geodesic open ball of radius r centered at z . That is, $\varphi(Z)$ is the radius of the largest geodesic ball that can be fitted on the surface \mathcal{X} without including any point of Z . The smaller $\varphi(Z)$, the finer the sampling set.

Given the smooth density ξ (on \mathcal{D}), we discretize it by first distributing n points $Z = \{z_i\}_{i=1}^n$ on \mathcal{X} with $\varphi(Z) = h > 0$. For $i = 1, \dots, n$, we define the sets Ξ_i to be the Voronoi cells corresponding to $z_i \in Z$; this gives a partition of the surface \mathcal{X} into disjoint convex sets, $\mathcal{X} = \cup_{i=1}^n \Xi_i$. We next define the discrete measure ξ_Z as a superposition of point measures localized in the points of Z , with weights given by the areas of Ξ_i , i.e. $\xi_Z = \sum_{i=1}^n \xi_i \delta_{z_i}$, with $\xi_i := \xi(\Xi_i) = \int_{\Xi_i} d\text{vol}_{\mathcal{X}}$. Similarly we denote by $W = \{w_j\}_{j=1}^p$, Υ_j , and $\zeta_j := \zeta(\Upsilon_j)$ the corresponding quantities for surface \mathcal{Y} . We shall always assume that the surfaces \mathcal{X} and \mathcal{Y} have the same area, which, for convenience, we can take to be 1. It then follows that the discrete measures ξ_Z and ζ_W have equal total mass (regardless of whether $n = p$ or not). The approximation algorithm will compute optimal transport for the discrete measures ξ_Z and ζ_W ; the corresponding discrete approximation to the distance between ξ and ζ is then given by $T_d^R(\xi_Z, \zeta_W)$.

Convergence of the discrete approximations $T_d^R(\xi_Z, \zeta_W)$ to $T_d^R(\xi, \zeta) = \mathbf{d}^R(\mathcal{X}, \mathcal{Y})$ as $\varphi(Z), \varphi(W) \rightarrow 0$ then follows from the results we prove in Appendix D. Theorem D.4 in Appendix D requires that the distance function $d_{\xi, \zeta}^R(\cdot, \cdot)$ used to define $T_d^R(\xi, \zeta)$ be uniformly continuous in its two arguments. This is indeed the case. As shown in [19], $d_{\xi, \zeta}^R(\cdot, \cdot)$ can be extended continuously to $\overline{\mathcal{D}} \times \overline{\mathcal{D}}$; this extension, which for convenience we continue to denote by $d_{\xi, \zeta}^R(\cdot, \cdot)$ is uniformly continuous: for all $\varepsilon > 0$, there exists a $\delta = \delta(\varepsilon)$ such that, for all $z, z' \in \mathcal{X}$, $w, w' \in \mathcal{Y}$,

$$d_{\mathcal{X}}(z, z') < \delta(\varepsilon), d_{\mathcal{Y}}(w, w') < \delta(\varepsilon) \Rightarrow |d_{\xi, \zeta}^R(z, w) - d_{\xi, \zeta}^R(z', w')| < \varepsilon,$$

where $d_{\mathcal{X}}(\cdot, \cdot)$ is the geodesic distance on \mathcal{X} , and $d_{\mathcal{Y}}(\cdot, \cdot)$ is the geodesic distance on \mathcal{Y} .

In Appendix D we prove that $\xi_Z \rightarrow \xi$ in the *weak* sense, as $\varphi(Z) \rightarrow 0$, i.e. that for all bounded continuous functions $f : \overline{\mathcal{D}} \rightarrow \mathbb{R}$, the convergence $\int_{\mathcal{D}} f d\xi_Z \rightarrow \int_{\mathcal{D}} f d\xi$ holds [24]. Similarly $\zeta_W \rightarrow \zeta$ in the weak sense as $\varphi(W) \rightarrow 0$. Furthermore, we prove that for $\max(\varphi(Z), \varphi(W)) < \frac{\delta(\varepsilon)}{2}$

$$|T_d^R(\xi_Z, \zeta_W) - T_d^R(\xi, \zeta)| < \varepsilon.$$

More generally, it is shown that

$$(2.2) \quad |T_d^R(\xi_Z, \zeta_W) - T_d^R(\xi, \zeta)| < \omega_{d_{\xi, \zeta}^R}(\max(\varphi(Z), \varphi(W))),$$

where $\omega_{d_{\xi, \zeta}^R}$ is the modulus of continuity of $d_{\xi, \zeta}^R$, that is

$$\omega_{d_{\xi, \zeta}^R}(t) = \sup_{d_{\mathcal{X}}(z, z') + d_{\mathcal{Y}}(w, w') < t} |d_{\xi, \zeta}^R(z, w) - d_{\xi, \zeta}^R(z', w')|.$$

We shall see below that it will be particularly useful to choose the centers in $Z = \{z_i\}_{i=1}^n$, $W = \{w_j\}_{j=1}^p$ such that the corresponding Voronoi cells are (approximately) of equal area, i.e. $n = N = p$ and $\xi_i = \xi(\Xi_i) \approx \frac{1}{N}$, $\zeta_j = \zeta(\Upsilon_j) \approx \frac{1}{N}$, where we have used that the total area of each surface is normalized to 1. An effective way to calculate such sample sets Z and W is to start from an initial random seed (which will not be included in the set), and take the geodesic point furthest from the seed as the initial point of the sample set. One then keeps repeating this procedure, selecting at each iteration the point that lies at the furthest geodesic distance from the set of points already selected. This algorithm is known as the Farthest Point Algorithm (FPS) [8]. An example of the output of this algorithm, using geodesic distances on a disk-type surface, is shown in Figure 3. Further discussion of practical aspects of Voronoi sampling of a surface can be found in [4].

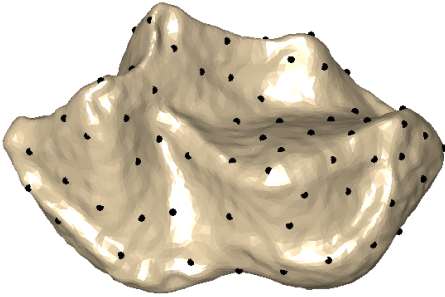


FIGURE 3. Sampling of the surface of Figure 1 obtained by the Farthest Point Algorithm.

2.3. Approximating the local distance function $d_{\mu, \nu}^R$. We are now ready to construct our discrete version of the optimal volume transportation for surfaces (1.2). The previous subsection describes how to derive the discrete measures μ_Z, ν_W and the sampling sets Z and W . For simplicity, we will, with some abuse of notation, identify the approximations of the conformal densities Γ_μ, Γ_ν with μ, ν . The approximation error made here is typically much smaller than the errors made in further steps (see below) and we shall neglect it. The final component is approximating $d_{\mu, \nu}^R(z_i, w_j)$ for all pairs $(z_i, w_j) \in Z \times W$. Applying (1.9) to the points z_i, w_j we have:

$$(2.3) \quad d_{\mu, \nu}^R(z_i, w_j) = \min_{m(z_i)=w_j} \int_{\Omega_{z_i, R}} |\mu(z) - \nu(m(z))| d\text{vol}_H.$$

To obtain $d_{\mu, \nu}^R(z_i, w_j)$ we will thus need to compute integrals over hyperbolic disks of radius R , which is done via a separate approximation procedure, set up once and for all in a preprocessing step at the start of the algorithm.

By using a Möbius transformation \tilde{m} such that $\tilde{m}(0) = z_0$, and the identity

$$\int_{\Omega_{z_0, R}} |\mu(\tilde{m}(u)) - \nu(m \circ \tilde{m}(u))| d\text{vol}_H(u) = \int_{\Omega_{z_0, R}} |\mu(z) - \nu(m(z))| d\text{vol}_H(z),$$

we can reduce the integrals over the hyperbolic disks $\Omega_{z_i, R}$ to integrals over a hyperbolic disk centered around zero.

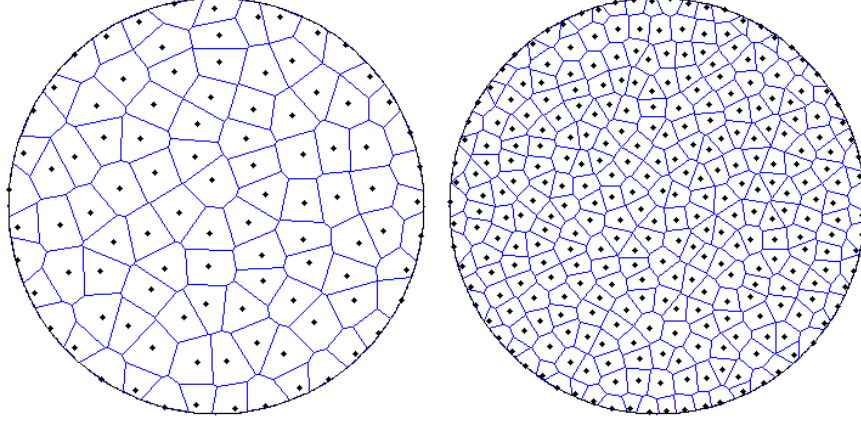


FIGURE 4. The integration centers and their corresponding Voronoi cells used for calculating the integration weights for the discrete quadrature. Left: 100 centers; Right: 300.

In order to (approximately) compute integrals over $\Omega_0 = \Omega_{0,R} = \{z \mid |z| \leq r_R\}$, we first pick a positive integer K and distribute centers $p_k, k = 1, \dots, K$ in Ω_0 . We then decompose Ω_0 into Voronoi cells Δ_k corresponding to the p_k , obtaining $\Omega_0 = \cup_{k=1}^K \Delta_k$; see Figure 4 (note that these Voronoi cells are completely independent of those used in 2.2.)

To approximate the integral of a continuous function f over Ω_0 we then use

$$\int_{\Omega_0} f(z) d\text{vol}_H(z) \approx \sum_k \left[\int_{\Delta_k} d\text{vol}_H(z) \right] f(p_k) = \sum_k \alpha_k f(p_k)$$

where $\alpha_k = \int_{\Delta_k} d\text{vol}_H(z)$.

We thus have the following approximation:

$$\begin{aligned} d_{\mu,\nu}^R(z_i, w_j) &= \min_{m(z_i)=w_j} \int_{\Omega_{z_i,R}} \left| \mu(z) - \nu(m(z)) \right| d\text{vol}_H(z) \\ &= \min_{m(z_i)=w_j} \int_{\Omega_{0,R}} \left| \mu(\tilde{m}_i(z)) - \nu(m(\tilde{m}_i(z))) \right| d\text{vol}_H(z) \\ (2.4) \qquad &\approx \min_{m(z_i)=w_j} \sum_k \alpha_k \left| \mu(\tilde{m}_i(p_k)) - \nu(m(\tilde{m}_i(p_k))) \right|, \end{aligned}$$

where the Möbius transformations \tilde{m}_i , mapping 0 to z_i , are selected as soon as the z_i themselves have been picked, and remain the same throughout the remainder of the algorithm.

It can be shown that picking a set of centers $\{p_k\}$ with fill-distance $h > 0$ leads to an $O(h)$ approximation; in Appendix A we prove:

Theorem 2.1. *For continuously differentiable μ, ν ,*

$$\left| d_{\mu,\nu}^R(z_i, w_j) - \min_{m(z_i)=w_j} \sum_k \alpha_k \left| \mu(\tilde{m}_i(p_k)) - \nu(m(\tilde{m}_i(p_k))) \right| \right| \leq C \varphi(\{p_k\}),$$

where the constant C depends only on μ, ν, R .

Let us denote this approximation by

$$\hat{d}_{\mu,\nu}^R(z_i, w_j) = \min_{m(z_i)=w_j} \sum_k \alpha_k \left| \mu(\tilde{m}_i(p_k)) - \nu(m(\tilde{m}_i(p_k))) \right|.$$

Since the above theorem guarantees that the approximation error $\left| \widehat{d}_{\mu,\nu}^R(z_i, w_j) - d_{\mu,\nu}^R(z_i, w_j) \right|$ can be uniformly bounded independently of z_i, w_j , it can be shown that

$$\left| T_d^R(\mu_Z, \nu_W) - T_{\widehat{d}}^R(\mu_Z, \nu_W) \right| \leq C\varphi(\{p_k\}),$$

where C is a (different) generic constant, dependent only upon μ, ν, R . Combining this with eq.(2.2) we get that

$$(2.5) \quad \left| T_d^R(\mu, \nu) - T_{\widehat{d}}^R(\mu_Z, \nu_W) \right| \leq \omega_{d_{\mu,\nu}^R}(\max(\varphi(Z), \varphi(W))) + C\varphi(\{p_k\}).$$

In practice, for calculating $\widehat{d}_{\mu,\nu}^R$, the minimization over M_{D, z_i, w_j} , the set of all Möbius transformations that map z_i to w_k , is discretized as well: instead of minimizing over all $m_{z_i, w_j, \sigma}$, we minimize over only the Möbius transformations $(m_{z_i, w_j, 2\pi\ell/L})_{\ell=0,1,\dots,L-1}$, where we use the following characterization of the disk-Möbius group:

Lemma 2.2. *For any $z_0, w_0 \in \mathcal{D}$, the set M_{D, z_0, w_0} constitutes a 1-parameter family of disk Möbius transformations, parametrized continuously over S^1 (the unit circle). More precisely, every $m \in M_{D, z_0, w_0}$ is of the form*

$$(2.6) \quad m(z) = \tau \frac{z - a}{1 - \bar{a}z}, \quad \text{with } a = a(z_0, w_0, \sigma) := \frac{z_0 - w_0 \bar{\sigma}}{1 - \bar{z}_0 w_0 \bar{\sigma}} \text{ and } \tau = \tau(z_0, w_0, \sigma) := \sigma \frac{1 - \bar{z}_0 w_0 \bar{\sigma}}{1 - z_0 \bar{w}_0 \sigma},$$

where $\sigma \in S_1 := \{z \in \mathbb{C}; |z| = 1\}$ can be chosen freely.

Taking this into account as well, we have thus

$$(2.7) \quad d_{\mu,\nu}^R(z_i, w_j) \approx \min_{\ell=1,\dots,L} \sum_k \alpha_k \left| \mu(\tilde{m}_i(p_k)) - \nu(m_{z_i, w_j, 2\pi\ell/L}(\tilde{m}_i(p_k))) \right|;$$

the error made in approximation (2.7) is therefore proportional to $L^{-1} + C\varphi(\{p_k\})$.

To summarize, our approximation $T_d^R(\mu_Z, \nu_W)$ to the uniformly continuous $T_d^R(\mu, \nu)$ proceeds in two steps: on the one hand, we compute the transportation cost between the discrete measures μ_Z, ν_W , approximating μ, ν ; on the other hand, this transportation cost involves a local distance $\widehat{d}_{\mu,\nu}^R$ which is itself an approximation. The transportation between the discrete measures will be computed by solving a linear programming optimization, as explained in detail in the next subsection. The final approximation error (2.5) depends on two factors: 1) the fill distances $\varphi(Z), \varphi(W)$ of the sample sets Z, W , and 2) the approximation of the local distance function $d_{\mu,\nu}^R(z_i, w_j)$ between the sample points. Combining the discretization of the Möbius search with (2.7), the total approximation error is thus proportional to $\omega_{d_{\mu,\nu}^R, \Gamma_\mu, \Gamma_\nu}(\varphi(\{p_k\})) + L^{-1} + \varphi(\{p_k\})$.

Recall that we are in fact using Γ_μ, Γ_ν in the role of μ, ν (see above), which entails an additional approximation error. This error relates to the accuracy with which discrete meshes approximate smooth manifolds, as well as the method used to approximate uniformization. We come back to this question in Appendix B. As far as we are aware, a full convergence result for (arbitrary) discrete uniformization is still unknown; in any case, we expect this error to be negligible (and approximately of the order of the largest edge in the full mesh) compared to the others.

2.4. Optimization via linear programming. The discrete formulation of eq. (1.2) is commonly formulated as follows:

$$(2.8) \quad \sum_{i,j} d_{ij} \pi_{ij} \rightarrow \min$$

$$(2.9) \quad \begin{cases} \sum_i \pi_{ij} = \nu_j \\ \sum_j \pi_{ij} = \mu_i \\ \pi_{ij} \geq 0 \end{cases},$$

where $\mu_i = \mu(\Xi_i)$ and $\nu_j = \nu(\Upsilon_j)$, and $d_{ij} = d_{\mu,\nu}^R(z_i, w_j)$.

In practice, surfaces are often only isometric in some (possibly large) parts. Furthermore, the sampled points may also fail to have a good one-to-one and onto correspondence (i.e. there typically are some points both in Z and in W that do not correspond well to any point in the other set). In these cases it is desirable to allow the algorithm to consider transportation plans π with marginals *smaller or equal* to μ and ν . Intuitively this means that we allow that only some fraction of the mass is transported and that the remainder can be “thrown away”. This leads to the following formulation:

$$(2.10) \quad \sum_{i,j} d_{ij} \pi_{ij} \rightarrow \min$$

$$(2.11) \quad \begin{cases} \sum_i \pi_{ij} \leq \nu_j \\ \sum_j \pi_{ij} \leq \mu_i \\ \sum_{i,j} \pi_{ij} = Q \\ \pi_{ij} \geq 0 \end{cases}$$

where $0 < Q \leq 1$ is a parameter set by the user that indicates how much mass *must* be transported, in total.

The corresponding transportation distance is defined by

$$(2.12) \quad T_d(\mu, \nu) = \sum_{ij} d_{ij} \pi_{ij},$$

where π_{ij} are the entries in the matrix π for the optimal (discrete) transportation plan.

Since these equations and constraints are all linear, we have the following theorem:

Theorem 2.3. *The equations (2.8)-(2.9) and (2.10)-(2.11) admit a global minimizer that can be computed in polynomial time, using standard linear-programming techniques.*

When correspondences between surfaces are sought, i.e. when one surface viewed as being transformed into the other, one is interested in restricting π to the class of permutation matrices instead of allowing all bistochastic matrices. (This means that each entry π_{ij} is either 0 or 1.) In this case the number of centers z_i must equal that of w_j , i.e. $n = N = p$, and it is best to pick the centers so that $\mu_i = \frac{1}{N} = \nu_j$, for all i, j . It turns out that these restrictions are sufficient to *guarantee* (without restricting the choice of π in any way) that the minimizing π is a permutation:

Theorem 2.4. *If $n = N = p$ and $\mu_i = \frac{1}{N} = \nu_j$, then*

- (1) *There exists a global minimizer of (2.8) that is a permutation matrix.*
- (2) *If furthermore $Q = \frac{M}{N}$, where $M < N$ is an integer, then there exists a global minimizer of (2.10) π such that $\pi_{ij} \in \{0, 1\}$ for each i, j .*

Remark 2.5. In the second case, where $\pi_{ij} \in \{0, 1\}$ for each i, j , and $\sum_{i,j=1}^N \pi_{ij} = M$, π can still be viewed as a permutation of M objects, “filled up with zeros”. That is, if the zero rows and columns of π (which must exist, by the pigeon hole principle) are removed, then the remaining $M \times M$ matrix is a permutation.

Proof. We first note that in both cases, we can simply renormalize each μ_i and ν_j by N , leading to the rescaled systems

$$(2.13) \quad \begin{cases} \sum_i \pi_{ij} = 1 \\ \sum_j \pi_{ij} = 1 \\ \pi_{ij} \geq 0 \end{cases} \quad \begin{cases} \sum_i \pi_{ij} \leq 1 \\ \sum_j \pi_{ij} \leq 1 \\ \sum_{i,j} \pi_{ij} = M \\ \pi_{ij} \geq 0 \end{cases}$$

To prove the first part, we note that the left system in (2.13) defines a convex polytope in the vector space of matrices that is exactly the Birkhoff polytope of bistochastic matrices. By the Birkhoff-Von Neumann

Theorem [17] every bistochastic matrix is a convex combination of the permutation matrices, i.e. each π satisfying the left system in (2.13) must be of the form $\sum_k c_k \tau^k$, where the τ^k are the $N!$ permutation matrices for N objects, and $\sum_k c_k = 1$, with $c_k \geq 0$. The minimizing π in this polytope for the linear functional (2.8) must thus be of this form as well. It follows that at least one τ^k must also minimize (2.8), since otherwise we would obtain the contradiction

$$(2.14) \quad \sum_{ij} d_{ij} \pi_{ij} = \sum_k c_k \left(\sum_{ij} d_{ij} \tau_{ij}^k \right) \geq \min_k \left\{ \sum_{ij} d_{ij} \tau_{ij}^k \right\} > \sum_{i,j} d_{ij} \pi_{ij} .$$

The second part can be proved along similar steps: the right system in (2.13) defines a convex polytope in the vector space of matrices; it follows that every matrix that satisfies the system of constraints is a convex combination of the extremal points of this polytope. It suffices to prove that these extreme points are exactly those matrices that satisfy the constraints and have entries that are either 0 or 1 (this is the analog of the Birkhoff-von Neumann theorem for this case; we prove this generalization in a lemma in Appendix C); the same argument as above then shows that there must be at least one extremal point where the linear functional (2.8) attains its minimum. \square

When we seek correspondences between two surfaces, there is thus no need to *impose* the (very nonlinear) constraint on π that it be a permutation matrix; one can simply use a (standard) linear program and Theorem 2.4 guaranteeing that the minimizer for the “relaxed” problem (2.8)-(2.9) or (2.10)-(2.11) is of the desired type if $n = N = p$ and $\mu_i = \frac{1}{N} = \nu_j$.

2.5. Consistency. In our schemes to compute the surface transportation distance, for example by solving (2.10), we have so far not included any constraints on the regularity of the resulting optimal transportation plan π^* . When computing the distance between a surface and a reasonable deformation of the same surface, one does indeed find, in practice, that the minimizing π^* is fairly smooth, because neighboring points have similar neighborhoods. There is no guarantee, however, that this has to happen. Moreover, we will be interested in comparing surfaces that are far from (almost) isometric, given by noisy datasets. Under such circumstances, the minimizing π^* may well “jump around”. In this subsection we propose a regularization procedure to avoid such behavior.

Computing how two surfaces best correspond makes use of the values of the “distances in similarity” $d_{\mu,\nu}^R(z_i, w_j)$ between pairs of points that “start” on one surface and “end” on the other; computing these values relies on finding a minimizing Möbius transformation for the functional (1.9). We can keep track of these minimizing Möbius transformations m_{ij} for the pairs of points (z_i, w_j) proposed for optimal correspondence by the optimal transport algorithm described above. Correspondence pairs (i, j) that truly participate in some close-to-isometry map will typically have Möbius transformations m_{ij} that are very similar. This suggests a method of filtering out possibly mismatched pairs, by retaining only the set of correspondences (i, j) that cluster together within the Möbius group.

There exist many ways to find clusters. In our applications, we gauge how far each Möbius transformation m_{ij} is from the others by computing a type of ℓ_1 variance:

$$(2.15) \quad E_V(i, j) = \sum_{(k,\ell)} \|m_{ij} - m_{k\ell}\| ,$$

where the norm is the Frobenius norm (also called the Hilbert-Schmidt norm) of the 2×2 complex matrices representing the Möbius transformations, after normalizing them to have determinant one. We then use $E_V(i, j)$ as a consistency measure of the corresponding pair (i, j) .

3. GENERALIZATION TO SPHERE-TYPE SURFACES

The above restriction to disk-type surfaces might seem somewhat limiting in practice. However, In this part of the paper we show how to easily generalize the ideas presented in [19] for other types of surfaces. We

choose to concentrate on the common case of sphere-type surfaces, that is, genus zero surfaces. We will start by making the necessary theoretical changes, and then we will present the numerical algorithm.

3.1. Generalization of the distance function. The Uniformization theory for sphere-type surfaces ensures a conformal 1-1 and onto mapping of the surface to the 2-sphere or equivalently to the extended complex plane $\widehat{\mathbb{C}} = \mathbb{C} \cup \{\infty\}$. The group of automorphisms, that is Möbius transformations $m : \widehat{\mathbb{C}} \rightarrow \widehat{\mathbb{C}}$ in this case is the collection of linear fractional transformations

$$(3.1) \quad m(z) = \frac{az + b}{cz + d},$$

where $a, b, c, d \in \mathbb{C}$ and $ad - bc \neq 0$.

The key observation that allows successful generalization in this case is that the choice of neighborhood $\Omega_{z_0, R}$ for a point z_0 should be made in a Möbius-invariant way. In contrast to hyperbolic geometry (and disk-preserving Möbius transformations) there is no Möbius-invariant distance function on the extended complex plane. Therefore, the neighborhoods should be chosen in a different way.

First, let us define the collection of *circles* in the extended complex plane with orientation by \mathcal{C} . That is, a circle $c \in \mathcal{C}$ is the set of complex points satisfying an equation of the type

$$Az\bar{z} + Bz + \overline{Bz} + D = 0,$$

where $A, D \in \mathbb{R}$ and $B \in \mathbb{C}$. By orientation of a circle $c \in \mathcal{C}$ we mean choosing the “inside” and “outside” parts of $\mathbb{C} \setminus c$. Note that this definition of “circle” includes straight lines that are circles through infinity (which is a legitimate point in the extended complex plane). Möbius transformations take circles to circles, and therefore we should choose our neighborhood of $z_0 \in \widehat{\mathbb{C}}$ from the collection of insides of circles \mathcal{C} . This choice should be: 1) well-defined and independent of the choices made in the Uniformization part (i.e., choice of Möbius transformation), 2) Robust to noise, and 3) characterized by a “size” parameter similar to R in the previous disk construction. For this latter “size” parameter we chose the area A of the circle neighborhood w.r.t the surface’s metric. Since we assume our surfaces have unit area, $A \in (0, 1]$. The neighborhood $\Omega_{z_0, A}$ is then defined to be the inside of the circle $c \in \mathcal{C}$ that contains the point z_0 (we use the orientation of c here) and has minimal circumference (in terms of the surface’s metric) among the collection of circles with insides that contain z_0 and have prescribed area A (in terms of the surface’s metric). In the generic case there is a unique such circle. (In cases where there is more than one such circle for a point z_0 it is possible to consider the discrete set of such minimal circles.) Since the neighborhoods $\Omega_{z_0, A}$ are chosen using solely intrinsic properties from the circle collection they are invariant to Möbius change of coordinates; in other words if two isometric surfaces \mathcal{M}, \mathcal{N} are compared at a pair of isometric points z_0, w_0 then the isometry mapping \mathcal{M} to \mathcal{N} is a Möbius transformation taking $\Omega_{z_0, A}$ to $\Omega_{w_0, A}$ as well as z_0 to w_0 .

Once the neighborhoods are set, the definition of $d_{\mu, \nu}^A(z_0, w_0)$ is straightforward: denote by M_{z_0, w_0}^A the collection of Möbius transformations m that take the interior of the circle $\Omega_{z_0, A}$ to the interior of $\Omega_{w_0, A}$, and for which $m(z_0) = w_0$. Similarly to the disk-preserving Möbius transformations this is one parameter subgroup parameterized over the unit circle (angle) $\theta \in [0, 2\pi)$. We then define

$$(3.2) \quad d_{\mu, \nu}^A(z_0, w_0) := \inf_{m \in M_{z_0, w_0}^A} \int_{\Omega_{z_0, A}} \left| 1 - \frac{\nu((m(z)) |m'(z)|^2)}{\mu(z)} \right| d\text{vol}_{\mathcal{M}}(z).$$

This is indeed the analog to eq. (1.9) for disk-type surfaces since both integrals can be written as

$$\int_{\Omega_{z_0, A}} \left\| \tilde{g}(z) - (m^* \tilde{h})(z) \right\|_{\tilde{g}} d\text{vol}_{\mathcal{M}}(z),$$

where \tilde{g} is the pull-back metric of \mathcal{M} on $\widehat{\mathbb{C}}$, and respectively \tilde{h} the pull-back metric of \mathcal{N} on $\widehat{\mathbb{C}}$, and the norm $\|\cdot\|_{\tilde{g}}$ is the standard one, induced by \tilde{g} , over the space of 2-covariant tensors.

Please note that the area-based definition of the neighborhoods used for the sphere-type case could also be used in the disk-type case; this would yield a unified definition for both cases. Basically, the choice of neighborhoods is a design choice left to the user; the difference between the new definition (above) and the old definition (hyperbolic geodesic disk) in the case of disk-type surfaces is that the old definition provides smaller neighborhoods near the boundary for disk type surfaces, while the new definition will maintain constant area neighborhoods even arbitrarily close to the surface’s boundary; depending on the application, one or the other selection may be preferable.

3.2. Numerical details. The algorithm for the sphere-type case is basically the same as for the disk-type; That is, we first sample N equally distributed points (in the sense described above) Z, W on the surfaces \mathcal{M}, \mathcal{N} (respectively). Second, the cost-distance function $d_{\mu, \nu}^A(z_i, w_j)$ is computed between every pair of sample points $(z_i, w_j) \in Z \times W$, and finally, a discrete mass-transportation problem is solved to output the distance and the correspondences. A few adjustments need to be made to this algorithm for the sphere-type case: 1) precomputing (approximating) the neighborhoods $\Omega_{z_i, A}, z_i \in Z$, and $\Omega_{w_j, A}, w_j \in W$ that are different from the hyperbolic geodesic disks used in the disk-type surface case, 2) representing the conformal density on the extended complex plane rather than the unit disk, and approximating the local distance $d_{\mu, \nu}^R(z_i, w_j)$. Next we describe these two adjustments in more detail.

Computing the neighborhoods $\Omega_{z_i, A}$. We describe the construction of neighborhoods $\Omega_{z_i, S}$ for every sample point $z_i \in Z$ in \mathcal{M} . The construction in \mathcal{N} is identical. We want to find the neighborhood $\Omega_{z_i, A}$ that is the interior of a conformal circle, has surface area A , and has minimal circumference compare to all other such circles. A circle is defined by a triplet of points z_i, z_j, z_k in the usual way. Adding the orientation, each triplet provides us with two choices of conformal circle neighborhoods. In our implementation we considered all $2\binom{N}{3}$ circles generated by the sample set Z . For each such circle (endowed with orientation) we estimate the surface area inscribed in it. If it is ϵ -close to the prescribed amount A we estimate its circumference on the surface. We define $\Omega_{z_i, A}$ the one with smallest circumference. Although theoretically the (globally) minimizing circle can fail to be unique this is a degenerate (and very rare) case, and so we ignore it.

Approximating $d_{\mu, \nu}^R(z_i, w_j)$. The second issue that arises when generalizing to sphere-type surfaces is the representation of the discrete conformal density $\Gamma_\mu(z), \Gamma_\nu(w)$. One option is to use spherical interpolation scheme and repeat the steps described in Section 2. However, one can also pick a different path that is very simple and offers an alternative to the smooth TPS approximation. The idea is to represent the conformal density by keeping track of a set of equally spreaded points on the surface $\tilde{Q} = \{\tilde{q}_\ell\}_{\ell=1}^{\mathcal{L}} \subset \mathcal{M}$ (similarly to Z), where each point represent a surface patch of size $\frac{1}{\mathcal{L}}$. In our implementation, we use this latter choice. We usually take a set of size $\mathcal{L} \approx 1000$. The discrete density is then represented on the extended sphere as $Q = \{q_\ell\}_{\ell=1}^{\mathcal{L}} = \Phi(\tilde{Q}) \subset \hat{\mathbb{C}}$. It can be shown that given a set $\Omega \subset \hat{\mathbb{C}}$ we have the approximation:

$$(3.3) \quad \left| \frac{1}{\mathcal{L}} \sum_{q_i \in \Omega} 1 - \int_{\Omega} d\text{vol}_{\mathcal{M}} \right| \leq C\varphi(\{\tilde{q}_\ell\}),$$

Figure 5 shows the density points spread on a cat model and on its uniformization sphere, as well as the neighborhood of a single point on the cat’s front leg. Denote by $P = \{p_\ell\}_{\ell=1}^{\mathcal{L}} \subset \hat{\mathbb{C}}$ the density points for surface N . To approximate $d_{\mu, \nu}^A(z_0, w_0)$ as defined in eq.(3.2) we follow the following steps: first, we map $Q \cap \Omega_{z_0, R}$ to the unit disk \mathcal{D} via a Möbius transformation that is defined by taking z_0 to the origin and $\Omega_{z_0, R}$ to the unit disk D . Denote the resulting unit disk points by Q_{z_0} . Similarly we map $P \cap \Omega_{w_0, R}$ to the unit disk (taking w_0 to the origin). We denote the resulting set by P_{w_0} . Second, for each $\theta \in \{0, \frac{2\pi}{L}, 2\frac{2\pi}{L}, \dots, (L-1)\frac{2\pi}{L}\}$ we rotate Q_{z_0} by θ around the origin, $e^{i\theta}Q_{z_0}$, and compare to the second density P_{w_0} . The way we compare the two densities is justified by eq. (3.3), that is we subdivide the unit disk (actually the entire square $[-1, 1]^2$) to bins and count, for each of the two densities $e^{i\theta}Q_{z_0}, P_{w_0}$ the number of points in each bin. Then, we can sum the absolute value of the difference to achieve our approximation to $d_{\mu, \nu}^A(z_0, w_0)$. Note that it is useful to convolve the bins’ structure with some kernel to spread the points (possibly smoothly) in several bins around the correct bin. In our experiments (presented in Section 5) we used a 30×30 bin structure

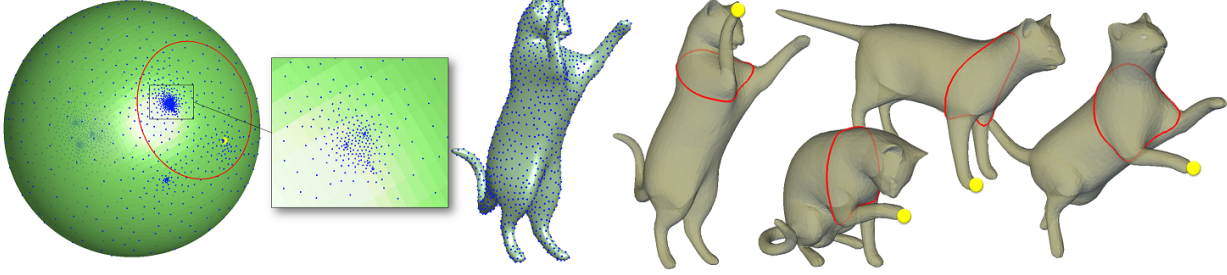


FIGURE 5. Sampling of the sphere-type cat surface (third from the left), and the sampling shown on the uniformization sphere (left). Note the zoom-in inset of the cat’s head. We also show the neighborhood (marked with red on the sphere) for $A = 0.3$ of a point (marked with yellow ball on the sphere) on the cat’s front leg (the model is taken from the Non-rigid World data-set [5]). On the right we show the neighborhood corresponding to the yellow point on the original cat surface model (fourth from the right) and on few other surfaces from the same class (the neighborhoods were computed independently in each surface). Note the invariance of this neighborhood under nearly-isometric deformations.

and convolved with the kernel $\frac{1}{9}(1, 1, 1) \otimes (1, 1, 1)$. Lastly, note that a similar convergence analysis to the one performed in Section 2 can be performed here, with similar results.

4. STABILITY

In this section we prove a result demonstrating how the new distance controls local distortion. We will prove it for the disk case, but similar arguments can be used for the sphere case. In this section we will use notations introduced in [19].

Theorem 4.1. *If $\mathbf{d}^R(\mathcal{M}, \mathcal{N})$ is small then the two surfaces are locally isometric: for sufficiently small $\mathbf{d}^R(\mathcal{M}, \mathcal{N})$ we can cover \mathcal{M} (minus an arbitrarily small boundary layer) with patches $\Omega_{z_0, R}$ and define mappings $f^{z_0} : \mathcal{M} \rightarrow \mathcal{N}$ (Möbius transformations) such that for all $z, z' \in \mathcal{M}$ (not very close to the boundary) with geodesic distance $d_g(z, z') \leq r(R)$, $r(R) > 0$, there exists a patch $\Omega_{z_0, R}$ such that $z, z' \in \Omega_{z_0, R} \cap \mathcal{M}$ and $f^{z_0}(\Omega_{z_0, R} \cap \mathcal{M}) \subset \Omega_{w_0, R} \cap \mathcal{N}$ such that:*

$$(4.1) \quad \left(1 - C_2 \mathbf{d}^R(\mathcal{M}, \mathcal{N})\right) d_g(z, z') \leq d_h(f^{z_0}(z), f^{z_0}(z')) \leq \left(1 + C_1 \mathbf{d}^R(\mathcal{M}, \mathcal{N})\right) d_g(z, z'),$$

where $d_g(z, z')$, $d_h(w, w')$ are the geodesic distance of $z, z' \in \mathcal{M}$ and $w, w' \in \mathcal{N}$, respectively, and $C_1, C_2 > 0$ are constants independent of the choice of z, z' .

Remark 4.2. Note that this result can be strengthened from *local isometric* to *isometric* by adding assumptions about the asymmetry of the considered surfaces (for example using arguments similar to those in [20]).

Proof. Fix $R > 0$, and let us consider a compact set $K \subset \mathcal{D}$. Let $C(R) = C(R; K, \mu) > 0$ be a constant such that $d_H(z, z') \leq C(R)d_g(z, z')$ for all $z, z' \in K$. Fix arbitrary $z, z' \in K$ such that $d_g(z, z') \leq \frac{R}{C(R)} := r(R)$ (so that $d_H(z, z') \leq R$).

Let $\mathbf{d}^R(\mathcal{M}, \mathcal{N}) = \varepsilon$. Consider the set

$$B = \{z_0 \mid \gamma_{z, z'} \subset \Omega_{z_0, R}\},$$

where $\gamma_{z, z'}$ is the set of points constituting the minimizing geodesic (in terms of the metric corresponding to surface \mathcal{M}) between z and z' . Note that the volume of this set on surface \mathcal{M} can be bounded from below $\text{vol}_{\mathcal{M}}(B) \geq \frac{1}{C_1} > 0$, for some constant $C_1 > 0$, independently of the choice of $z, z' \in K$.

Next, denote by π^* the optimal transportation plan realizing the minimal transportation cost, then:

$$\begin{aligned} \varepsilon &\geq \int_{\mathcal{D} \times \mathcal{D}} d_{\mu, \nu}^R(z, w) d\pi^*(z, w) \\ &\geq \int_{B \times \mathcal{D}} d_{\mu, \nu}^R(z, w) d\pi^*(z, w) \\ &\geq \min_{(z, w) \in B \times \mathcal{D}} [d_{\mu, \nu}^R(z, w)] \int_{B \times \mathcal{D}} d\pi^*(z, w) = \min_{(z, w) \in B \times \mathcal{D}} [d_{\mu, \nu}^R(z, w)] \text{vol}_{\mathcal{M}}(B). \end{aligned}$$

Hence there exists $z_0 \in B$ and $w_0 \in \mathcal{D}$ such that

$$d_{\mu, \nu}^R(z_0, w_0) \leq \frac{\varepsilon}{\text{vol}_{\mathcal{M}}(B)} \leq C_1 \varepsilon.$$

Next, remember that

$$d_{\mu, \nu}^R(z_0, w_0) = \inf_{m \in M_{\mathcal{D}}, m(z_0) = w_0} \int_{\Omega_{z_0, R}} \|\tilde{\mu} - m^* \tilde{\nu}\|_{g(z)} d\text{vol}_{\mathcal{M}}(z).$$

Since $s(z) = \|\tilde{\mu} - m^* \tilde{\nu}\|_{g(z)}$ is Lipschitz as a function of argument z (since $\tilde{\mu}, \tilde{\nu}$ are smooth and positive on compact domain, and m is analytic) there exists some constant $C_2 > 0$, and a Möbius transformation m such that

$$(4.2) \quad \max_{z \in \Omega_{z_0, R}} \|\tilde{\mu} - m^* \tilde{\nu}\|_{g(z)} \leq C_1 C_2 \varepsilon.$$

Set $f^{z_0} : \mathcal{M} \cap \Omega_{z_0, R} \rightarrow \mathcal{M} \cap \Omega_{w_0, R}$ to be the restriction of this m to $\Omega_{z_0, R}$.

Let $z \in \mathcal{M} \cap \Omega_{z_0, R}$ (we identify (\mathcal{M}, g) with $(\mathcal{D}, \tilde{\mu})$), and $w \in \mathcal{N} \cap \Omega_{w_0, R}$. Further take $e_1, e_2 \in T_z \mathcal{M}$ orthonormal. That is,

$$(4.3) \quad e_k^i e_\ell^j g_{ij} = e_k^i e_\ell^j \tilde{\mu}(z) \delta_{i,j} = \delta_{k,\ell}.$$

Similarly we take orthonormal b_1, b_2 in $T_w \mathcal{N}$. We will denote the matrix $[Df_z] = [Df]$ representing the differential of f at the point z , Df_z , in the bases $E = \{e_1, e_2\}$, $B = \{b_1, b_2\}$. Then writing the singular value decomposition of $[Df]$ we have

$$[Df] = Q \text{diag}(\sigma_1(z), \sigma_2(z)) R^T,$$

where Q, R are orthogonal and $\sigma_1 \leq \sigma_2$ are the respective singular values. Then we have

$$(4.4) \quad \|\tilde{\mu} - f^* \tilde{\nu}\|_{g(z)}^2 = \|Id - [Df]^t [Df]\|_F^2 = (1 - \sigma_1(z))^2 + (1 - \sigma_2(z))^2,$$

where Id is the identity 2×2 matrix, and $\|\cdot\|_F$ denotes the Frobenius norm. Using (4.2), (4.4) we get

$$|1 - \sigma_2(z)| \leq C_1 C_2 \varepsilon.$$

Since obviously from this last bound $\sigma_2(z)$ for $z \in \Omega_{z_0, R}$ is bounded there exists a constant $C_3 > 0$ such that

$$0 \leq \sigma_2(z) \leq 1 + C_3 \varepsilon.$$

Taking $\gamma_{z, z'}(t) : [0, 1] \rightarrow \mathcal{M}$ to be the minimizing geodesic between the points $\gamma_{z, z'}(0) = z$, and $\gamma_{z, z'}(1) = z'$, and since the induced norm $\|[Df_z]\| \leq \sigma_2(z)$ for $z \in \Omega_{z_0, R} \supset \gamma_{z, z'}$, we have:

$$\begin{aligned} d_h(f(z), f(z')) &\leq \int_0^1 \left\| \frac{d}{dt} f(\gamma_{z, z'}(t)) \right\|_h dt \\ &\leq \int_0^1 \|[Df]\| \|\dot{\gamma}_{z, z'}(t)\|_g dt \\ (4.5) \quad &\leq \max_{z \in \gamma_{z, z'}} \|[Df(z)]\| d_g(z, z') \\ &\leq (1 + C_3 \varepsilon) d_g(z, z') \\ &= \left(1 + C_3 \mathbf{d}^R(\mathcal{M}, \mathcal{N})\right) d_g(z, z'). \end{aligned}$$

The second direction is achieved using the fact that $\| [Df_z]^{-1} \| \leq \frac{1}{\sigma_1(z)}$ and therefore from (4.2),(4.4) we get

$$0 \leq \frac{1}{\sigma_1(z)} \leq 1 + C_4\varepsilon,$$

for some constant $C_4 > 0$. Next, similarly to above:

$$\begin{aligned} d_g(f^{-1}(f(z)), f^{-1}(f(z'))) &= \int_0^1 \left\| \frac{d}{dt} f^{-1}(\gamma_{f(z), f(z')}(t)) \right\|_g dt \\ &\leq \int_0^1 \| [Df^{-1}] \| \| \dot{\gamma}_{f(z), f(z')}(t) \|_h dt \\ (4.6) \quad &\leq \max_{w \in \gamma_{f(z), f(z')}} \| [Df(w)]^{-1} \| d_h(f(z), f(z')) \\ &\leq (1 + C_4\varepsilon) d_h(f(z), f(z')) \\ &= \left(1 + C_4 \mathbf{d}^R(\mathcal{M}, \mathcal{N}) \right) d_h(f(z), f(z')). \end{aligned}$$

Combining (4.5),(4.6) we achieve the result. □

5. EXPERIMENTAL VALIDATION AND COMMENTS

In this section we perform experimental validation of our algorithms. We have tested and experimented with our algorithms on four different data-sets:

- (1) *Non-rigid World data-set* [5]. This data-set was distributed by Bronstein, Bronstein and Kimmel and was specifically constructed for evaluating shape comparison algorithms in the scenario of non-rigid shapes; it contains meshes of different objects (cats, dogs, wolves, humans, etc...) in different poses. We compare our results on this data-set to the Gromov-Hausdorff algorithm suggested in [1, 5].
- (2) *SHREC 2007 Watertight Benchmark* [10] This data-set contains meshes of several objects within a given *semantic* class for several different classes, such as chairs, 4-legged animals, humans, etc... It is more challenging for isometric-invariant matching algorithms since most of the objects are far from isometric to the objects in the same semantic class, for example the 4-legged animals class contains a giraffe and a dog.
- (3) *Synthetic*. We constructed this data-set to test the effect of the “size” parameter R on the distance behavior.
- (4) *Primate molar teeth*. This data-set originates from a real biological problem/application; it consists of molar teeth surface for different primates. It was communicated to us by biologists who compare these shapes for characterization and classification of mammals.

Remark 5.1. For all data-sets, we scaled the meshes to have unit area, because our goal is to compare surfaces solely based on shape, regardless of size.

Non-rigid World data-set and comparison to Gromov-Hausdorff-type distance. In the first experiment we ran our sphere-type algorithm to determine conformal Wasserstein distances for all pairs in the Non-rigid World data-set, distributed by Bronstein, Bronstein and Kimmel [1, 5, 4]; we compare the results to those obtained using the code for the (symmetrized) partial embedding Gromov-Hausdorff (speGH) distance distributed by the same authors. The speGH distance has been used with great success in surface comparison [1, 5, 4] and can handle situations beyond the scope of our, more limited algorithm, it can e.g., compare surfaces of different genus. We therefore consider it as a state-of-the-art algorithm. In order to compare our Conformal Wasserstein distance with speGH for applications of interest to us, we use both algorithms on Non-rigid World data-set where all the surfaces are scaled to have unit area and where 100 sample points are chosen on each surface.

The Non-rigid World data-set contains meshes of different poses of the following articulated objects: a centaur, a cat, a dog, a horse, a human female, and two human males (“Michael” and “David”).

The two resulting dissimilarity matrices are shown in Figure 6 (a,d). The dissimilarity matrices are both normalized by translating the minimal value to zero and scaling the maximal value to one. The color scheme is Matlab’s “Jet” where dark blue represents low (close to zero) value, and dark red indicates high (close to one) values. The Sphere-type algorithm used $A = 0.3$, and a 30×30 bins discretization with the convolution kernel $(1, 1, 1) \otimes (1, 1, 1)$ (all the sphere-type examples use these bin settings) to obtain the discretizations of the conformal density. The timing for running one comparison $\mathbf{d}^A(\mathcal{M}, \mathcal{N})$ was 90 seconds on 2.2GHz AMD Opteron processor. Figure 6 (b-c) and (e-f) shows two nearest neighbors classifications tests where a white square inside a dark-red area means success and white square on black area is a failure.

The structure of the dissimilarity matrix is illustrated in the two plots in Figure 7. Figure 7 (a) shows the classification rates as a function of the number K of nearest neighbors, where for each fixed K we calculated the classification rate as follows. For each object we counted how many from its K -nearest neighbors are of the same class. We summed all these numbers and divided by the total number of possible correct classifications. The blue curve shows the analysis of the dissimilarity matrix output by our distance algorithm and the red curve by the speGH distance code. In (b) we show the ROC curve where for every $K = 1, 2, \dots, 10$ we plot the True Positive Rate (TPR), that is the number of true positives divided by the number of positives, as a function of the False Positive Rate (FPR), that is the number of false positives divided by the number of negatives.

SHREC 2007 Watertight Benchmark [10]. Our next experiment deals with a data-set with larger in-class variations; SHREC 2007 contains 20 categories of models with 20 meshes for each category (400 meshes in total) the categories are, e.g., chairs, 4-legged animals, humans, planes, tables, etc...

For our experiment, we restricted ourselves to all the meshes of 8 categories that contained only surfaces of genus zero (since our current algorithm does not support surfaces of higher genus) and that seemed intrinsically similar; these categories were: humans, 4-legged animals, ants, hands, airplanes, teddy-bears, pliers, Armadillos. We ran our sphere-type algorithm to compute the distance between all pairs. We tested the “size” parameters $A = 0.3, 0.4, 0.5$. The bin was the same as for the previous data-set. However, to achieve faster running times (we had about 25,000 comparisons...) we took only 50 sample points. The running time for one pair of objects was around 15 seconds.

Figure 8 shows the dissimilarity matrices (top row) using the three different values if A : 0.3, 0.4, 0.5, and the dissimilarity matrix resulting from combining them:

$$T_d(\mu, \nu) = T_d^{0.3}(\mu, \nu) \cdot T_d^{0.4}(\mu, \nu) \cdot T_d^{0.5}(\mu, \nu).$$

Note that $T_d(\mu, \nu)$ is also a metric and suggests a way to remove the influence of the size parameter if desired. The combined distance produced the best classification results as seen in the bottom row, where for each row the white square shows the nearest neighbor to that object. The dark red areas represent the different categories. The combined distance reached the very high classification rate of 95% on this challenging data-set. Figure 9 shows for one object in each category its four closest neighbors. Note the non-rigid nature of some of the objects (e.g., humans, hands), and the substantial deviation from perfect isometry within class (e.g., 4-legged animals). Figure 10 demonstrates a partial failure case where although the first two nearest neighbors to the Giraffe are within the 4-legged animals category, the third nearest neighbor is the one-armed armadillo, which belong to a different category (remember that the algorithm is size invariant).

Synthetic data-set. This experiment was designed to test the influence of the size parameter R on the behavior of the distance. The surfaces we compared are shown in the top row of Figure 11, they each have three small bumps, in different positions. At first sight, one might think that for small R , the distance $\mathbf{d}^R(\mathcal{M}, \mathcal{N})$ based on comparing neighborhoods of “size” R , would have trouble distinguishing these objects from each other. However, one should keep in mind that the uniformization process is a global one: changing the metric in one region of the surface would effect the uniformization of other regions (but influence would decay like appropriate Green’s function). Figure 11 plot the distance of disk-type model A to the four others, for different R values. We also show hyperbolic neighborhoods corresponding to the three different size parameters (color coded the same way as the graphs). We scaled the distances to have maximum

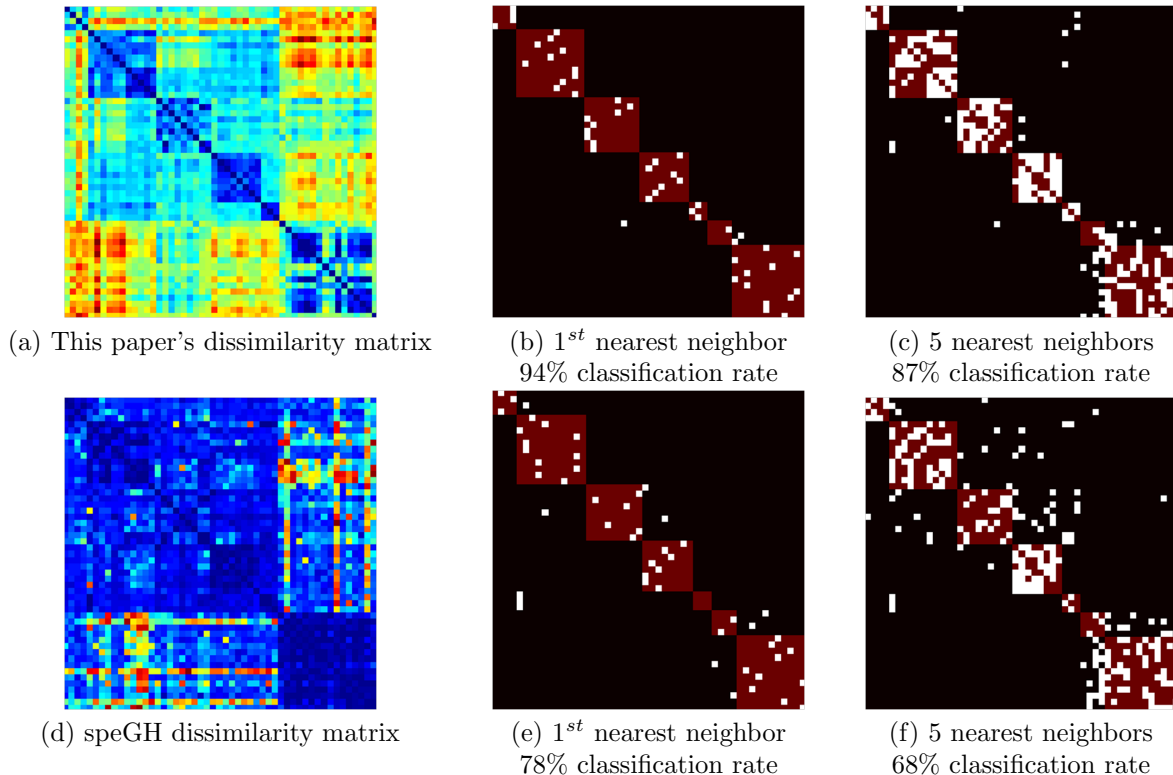


FIGURE 6. The dissimilarity matrices for the unit area scaled Non-rigid World data-set [1, 5] calculated with the conformal Wasserstein (CW) distance given by our algorithm (a) and the symmetric partial-embedding Gromov-Hausdorff (speGH) distance [1, 5] (d). In the second column (b,e) we show the ground truth classification matrix (dark-red) and the first nearest neighbor (white) according to the CW (in b) and to the speGH (in e) distance for each row. The third column (c,f) shows the five nearest neighbors (when there are fewer than five in some category we simply limit ourselves to the number in that category). Note that white squares should be in dark red regions to indicate correct classification. Note that with only 100 sampling points, “Michael” and “David” are not distinguishable, so if a pose of Michael is among the nearest neighbors of a pose of David, we still count it as a correct classification.

of one (since smaller R results naturally in smaller distances). Note that even the smallest size value $R = 0.25$ already distinguishes between the different models. Further note, that larger size parameters such as $R = 0.75$ results in slightly more intuitive linear distance behavior. Overall, the size parameter R does affect the distance, but not in a very significant way.

Primate molar teeth. Finally, we present a few experimental results related to a biological application; in a case study of the use of our approach to the characterization of mammals by the surfaces of their molars, we compare high resolution scans of the masticating surfaces of molars of several lemurs, which are small primates living in Madagascar. Traditionally, biologists specializing in this area carefully determine landmarks on the tooth surfaces, and measure characteristic distances and angles involving these landmarks. A first stage of comparing different tooth surfaces is to identify correspondences between landmarks. Figure 12 illustrates how $d_{\mu,\nu}^R(z,w)$ (disk-type) can be used to find corresponding pairs of points on two surfaces by showing both a “good” and a “bad” corresponding pair. The left two columns of the figure show the pair of points in each case; the two middle columns show the best fit after applying the minimizing Möbius on the corresponding disk representations; the rightmost column plots $\int_{\Omega_{z_0,R}} |\mu(z) - (m_{z_0,w_0,\sigma\nu}^*(z))| d\text{vol}_H(z)$,

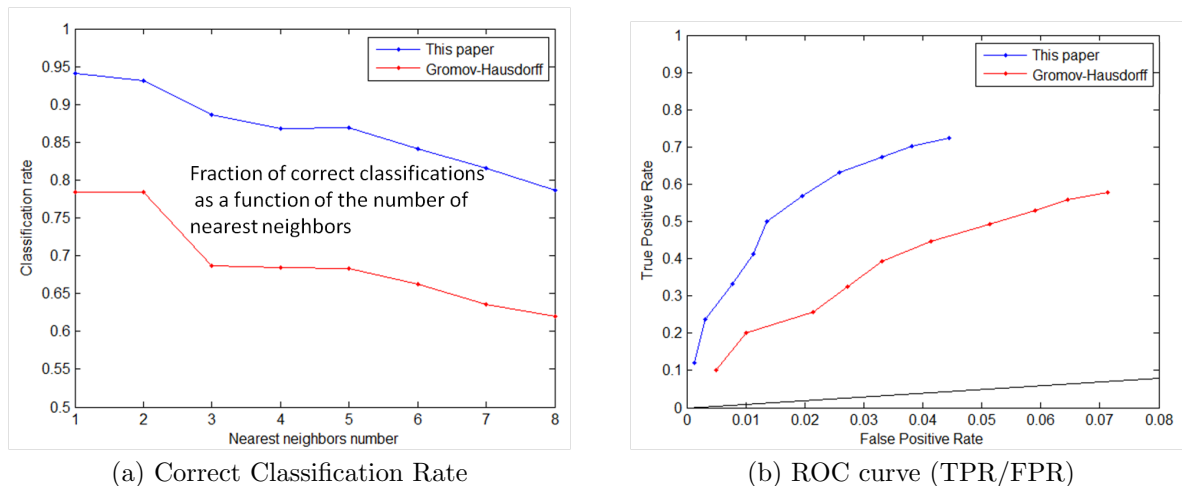


FIGURE 7. Correct Classification Rate and ROC curves for the dissimilarity matrices produces by our method (blue) and Gromov-Hausdorff-type metric (red). See text for details.

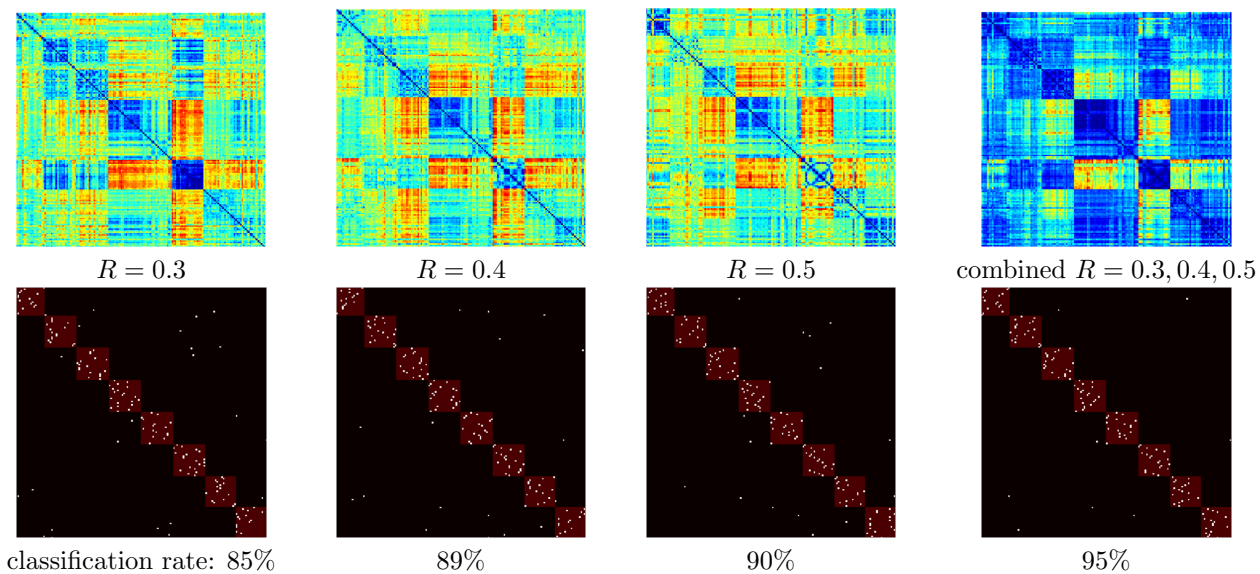


FIGURE 8. Dissimilarity matrices (top row) for the SHREC 2007 watertight Benchmark [10] with different size parameter: $R = 0.3, 0.4, 0.5$ and their combination (see text for details). Bottom row shows the first nearest neighbor classification test where white squares denote the nearest neighbor of that row’s object and the dark red area represent correct category classification.

the value of the “error”, as a function of parameter σ , parametrizing the Möbius transformations that map a give point z_0 to another given point w_0 (see Lemma 2.2). The “best” corresponding point w_0 for a given z_0 is the one that produces the lowest minimal value for the error, i.e. the lowest $d_{\mu,\nu}^R(z_0, w_0)$.

Figure 13 show the top 120 most consistent corresponding pairs (in groups of 20) for two molars belonging to lemurs of different species. Corresponding pairs are indicated by highlighted points of the same color.

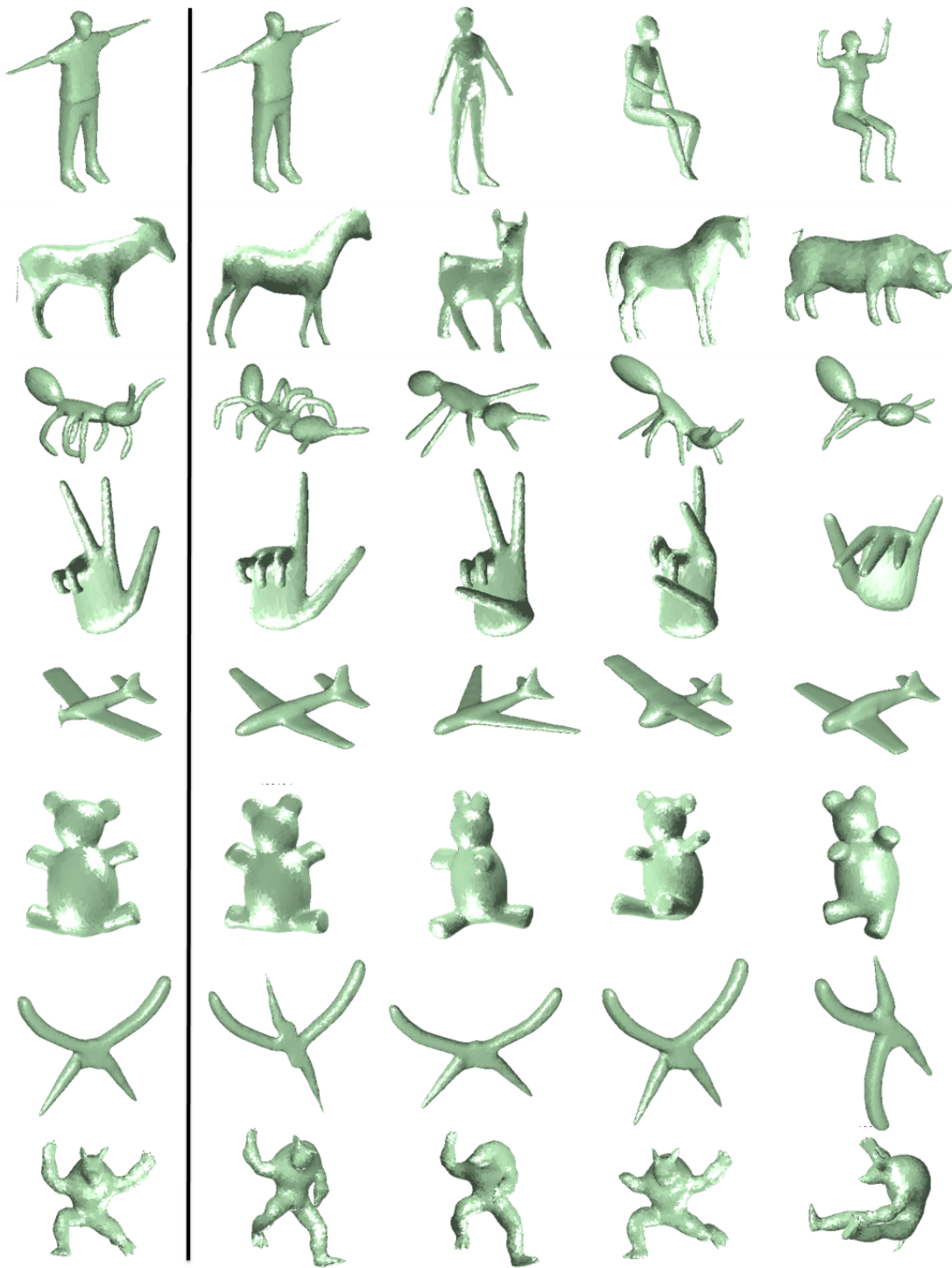


FIGURE 9. SHREC 2007 watertight Benchmark [10]: we show the four closest neighbors to each of the objects on the left side (we show one example from each category).

These correspondences have surprised the biologists from whom we obtained the data sets; their experimental measuring work, which incorporates finely balanced judgment calls, had defied earlier automatization attempts.

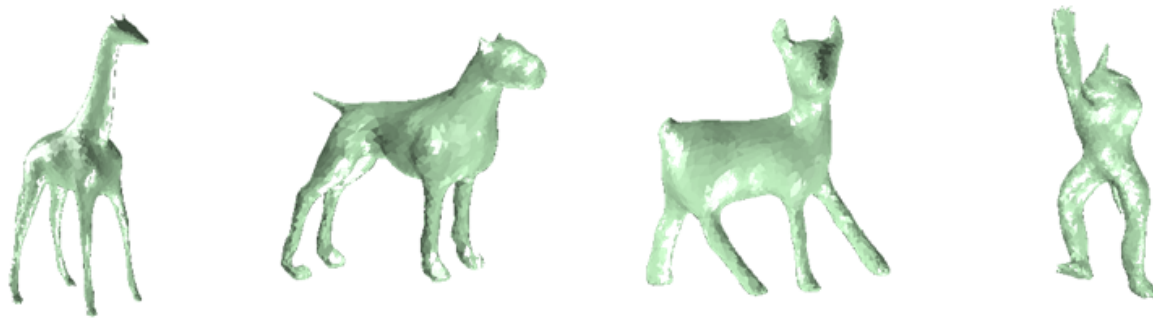


FIGURE 10. SHREC 2007 watertight Benchmark [10]: a partially failure case where the giraffe has correct two nearest neighbors, however its 3rd nearest neighbor is a one armed armadillo. Remember that our matching is scale invariant.

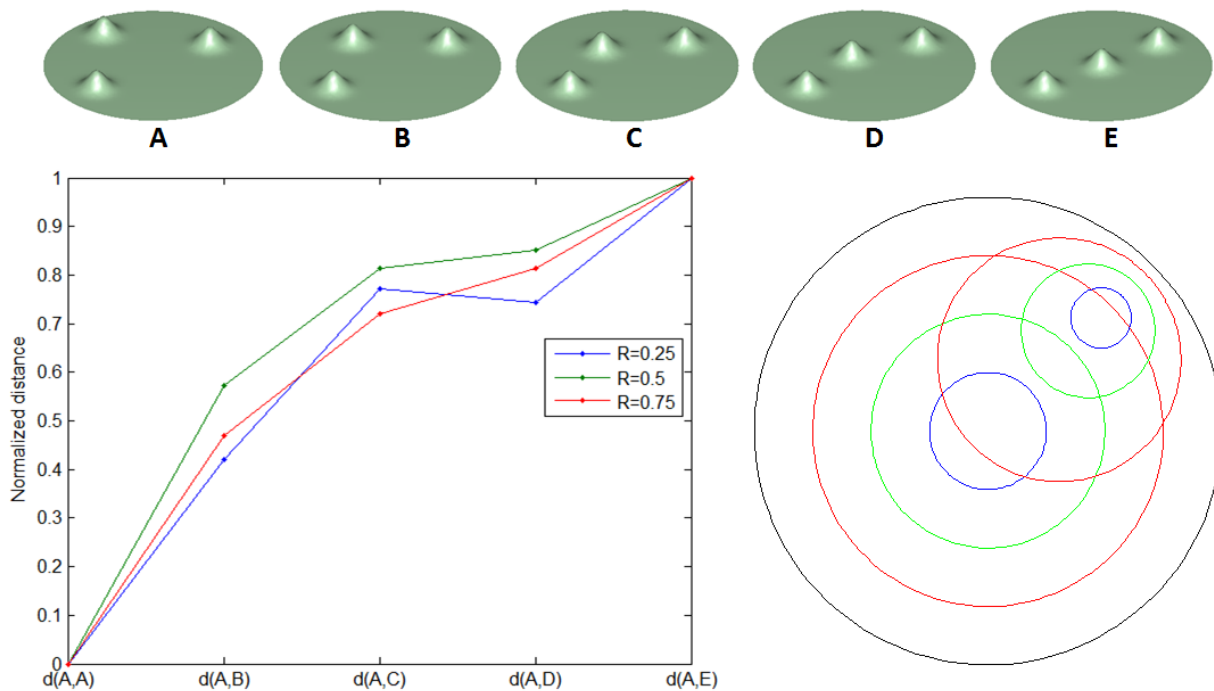


FIGURE 11. Testing influence of the size parameter R to sperate identical models with small features. We compare the distances of the disk model marked with A to all other models $A - E$ using three different size parameters $R = 0.25, 0.5, 0.75$. We also show examples of hyperbolic disk of these radiuses as used by our disk-type algorithm (the are color coded like the graph lines).

Once the differences and similarities between molars from different animals have been quantified, they can be used (as part of an approach) to classify the different individuals. Figure 14 illustrates a preliminary result that illustrates the possibility of such classifications based on the distance operator between surfaces introduced in this paper. The figure illustrates the pairwise distance matrix for eight molars, coming from individuals in four different species (indicated by color). The clustering was based on only the distances

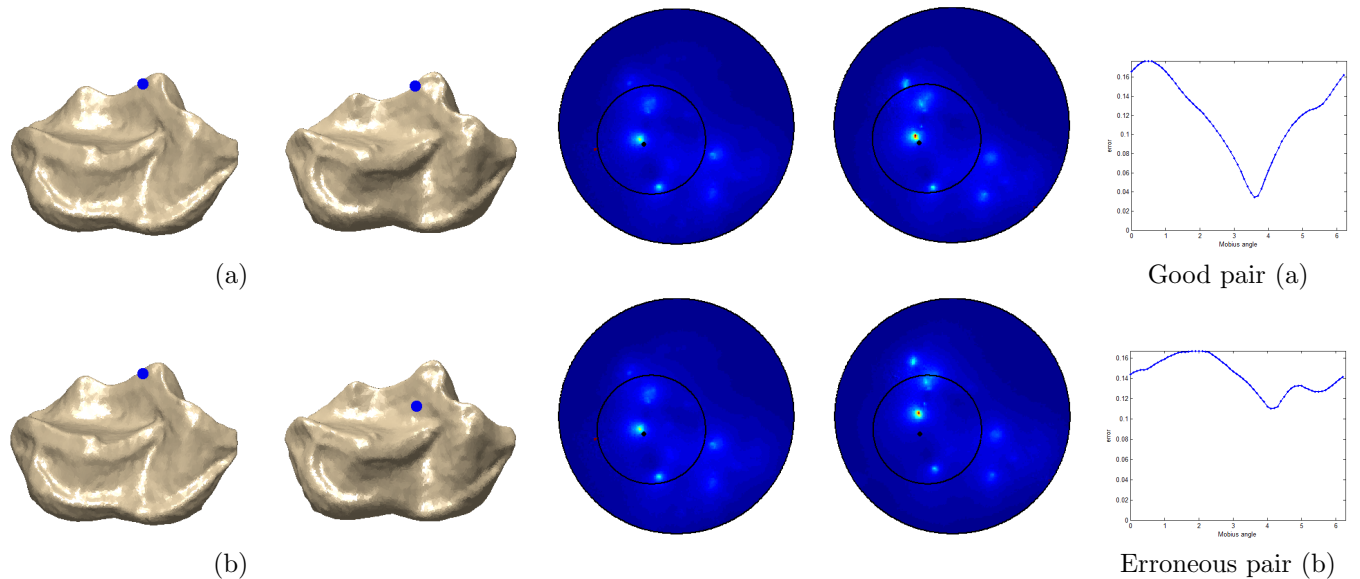


FIGURE 12. Calculation of the local distance $d_{\mu,\nu}^R(\cdot, \cdot)$ between pairs of points on two different surfaces (each row shows a different pair of points; the two surfaces are the same in the top and bottom rows). The first row shows a “good” pair of points together with the alignment of the conformal densities $\mu, m^*\nu$ based on the best Möbius transformation m minimizing $\int_{\mathcal{D}} \|\tilde{\mu} - m^*\tilde{\nu}\| d\text{vol}_{\mathcal{M}}$. The plot of this latter integral as a function of m (parameterized by $\sigma \in [0, 2\pi)$, see (1.5)) is shown in the right-most column. The second row shows a “bad” correspondence which indeed leads to a higher local distance $d_{\mu,\nu}^R$.

between the molar surfaces; it clearly agrees with the clustering by species, as communicated to us by the biologists from whom we obtained the data sets.

One final comment regarding the computational complexity of our method. There are two main parts: the preparation of the distance matrix d_{ij} and the linear programming optimization. For the linear programming part we used a Matlab interior point implementation with N^2 unknowns, where N is the number of points spread on the surfaces. In our experiments, the optimization typically terminated after 15 – 20 iterations for $N = 150 - 200$ points, which took about 2-3 seconds. The computation of the similarity distance d_{ij} took longer, and was the bottleneck in our experiments. We separate the disk-type and the sphere-type algorithms.

For the sphere-type algorithm if we use $N = \mathcal{L}$ sample points (Q) on each surface then for each pair we compare the difference (using fixed size bin structure) of the discrete conformal densities for fixed number of Möbius transformations. This results in $O(N^3)$ algorithm for computing the distance matrix d_{ij} . In our experiments the total distance computation time (including linear programming optimization) was around 15 seconds for $N = \mathcal{L} = 50$ (in the SHREC 2007 data-set), to 90 second per comparison for $N = \mathcal{N} = 100$ (in the Non-rigid world data-set). In the sphere-type examples we have used 2.2GHz AMD Opteron processor. The sphere-type algorithm was coded completely in Matlab and was not optimized.

For the disk-type algorithm, if we spread N points on each surface, and use them all (which was usually not necessary) to interpolate the conformal factors $\Gamma_{\mu}, \Gamma_{\nu}$, if we use P points in the integration rule, and take L points in the Möbius discretization (see Section 2 for details) then each approximation of $d_{\mu,\nu}^R(z_i, w_j)$ by (2.7) requires $O(L \cdot P \cdot N)$ calculations, as each evaluation of $\Gamma_{\mu}, \Gamma_{\nu}$ takes $O(N)$ and we need $L \cdot P$ of those. Since we have $O(N^2)$ distances to compute, the computation complexity for calculating the similarity distance matrix d_{ij} is $O(L \cdot P \cdot N^3)$. This step was coded in C++ (and therefore the time difference to the sphere-type case) and took 3.5 seconds for $N = 50$, 51 seconds for $N = 100$, under 5 minutes for $N = 150$

and two hours for $N = 300$ (in these examples we took $P \approx N$). However, also in this case we have not optimized the algorithm and we believe these times can be reduced significantly. The disk-type algorithm ran on Intel Xeon (X5650) 2.67GHz processor.

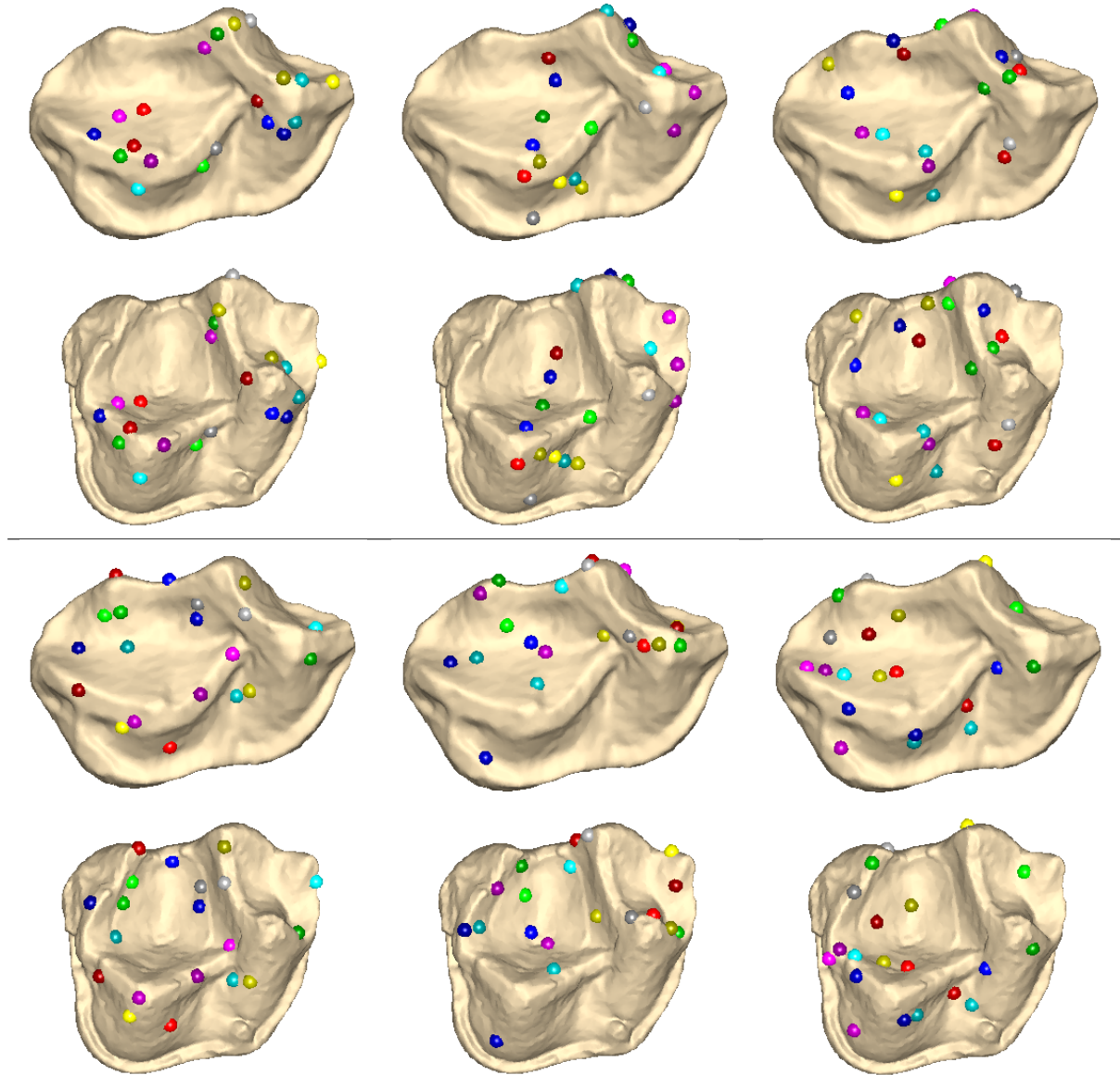


FIGURE 13. The top 120 most consistent corresponding pairs between two molar teeth models.

6. ACKNOWLEDGMENTS

The authors would like to thank Cédric Villani and Thomas Funkhouser for valuable discussions. We are grateful to Jukka Jernvall, Stephen King, and Doug Boyer for providing us with the tooth data sets, and for many interesting comments. We would like to thank the anonymous reviewers that challenged us to improve our manuscript with excellent comments and suggestions. ID gratefully acknowledges (partial) support for this work by NSF grant DMS-0914892, and by an AFOSR Complex Networks grant; YL thanks the Rothschild foundation for postdoctoral fellowship support.

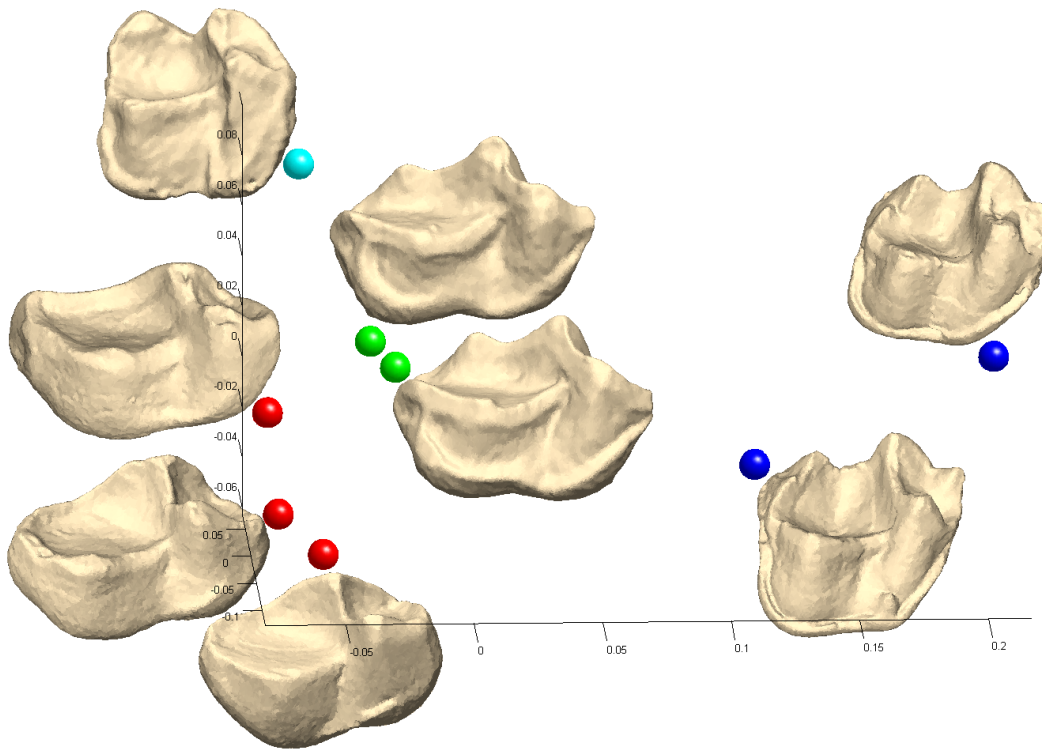


FIGURE 14. Embedding of the distance graph of eight teeth models using multi-dimensional scaling. Different colors represent different lemur species. The graph suggests that the geometry of the teeth might suffice to classify species.

REFERENCES

1. R. Kimmel, A. M. Bronstein, M. M. Bronstein, *Generalized multidimensional scaling: a framework for isometry-invariant partial surface matching*, Proc. National Academy of Sciences (PNAS) **103** (2006), no. 5, 1168–1172.
2. Mikael Fortelius, Jukka Jernvall, Alistair R. Evans, Gregory P. Wilson, *High-level similarity of dentitions in carnivores and rodents*, Nature **445** (2007), 78–81.
3. Susanne C. Brenner and L. Ridgway Scott, *The mathematical theory of finite element methods*, third ed., Texts in applied mathematics, vol. 15, 2008.
4. Alexander Bronstein, Michael Bronstein, and Ron Kimmel, *Calculus of nonrigid surfaces for geometry and texture manipulation*, IEEE Transactions on Visualization and Computer Graphics **13** (2007), no. 5, 902–913.
5. Alexander M. Bronstein, Michael M. Bronstein, and Ron Kimmel, *Efficient computation of isometry-invariant distances between surfaces*, SIAM J. Sci. Comput. **28** (2006), no. 5, 1812–1836.
6. E. Cella, *The quadratic assignment problem: Theory and algorithms (combinatorial optimization)*, Springer, 1998.
7. Gerhard Dziuk, *Finite elements for the Beltrami operator on arbitrary surfaces*, vol. 1357, Springer Berlin / Heidelberg, 1988.
8. Y. Eldar, M. Lindenbaum, M. Porat, and Y. Zeevi, *The farthest point strategy for progressive image sampling*, 1997.
9. Bruce Fischl, Martin I. Sereno, Roger B. H. Tootell, and Anders M. Dale, *High-resolution intersubject averaging and a coordinate system for the cortical surface*, Hum. Brain Mapp **8** (1999), 272–284.
10. Daniela Giorgi, Silvia Biasotti, and Laura Paraboschi, *SHREC:SHape REtrieval Contest: Watertight models track*, <http://watertight.ge.imati.cnr.it/>, 2007.
11. Mikhail Gromov, M. Katz, P. Pansu, and S. Semmes, *Metric structures for riemannian and non-riemannian spaces*, Birkhäuser Boston, December 2006.
12. Xianfeng Gu and Shing-Tung Yau, *Global conformal surface parameterization*, SGP '03: Proceedings of the 2003 Eurographics/ACM SIGGRAPH symposium on Geometry processing (Aire-la-Ville, Switzerland, Switzerland), Eurographics Association, 2003, pp. 127–137.
13. Steven Haker, Lei Zhu, Allen Tannenbaum, and Sigurd Angenent, *Optimal mass transport for registration and warping*, International Journal on Computer Vision **60** (2004), 225–240.

14. Irwin Kra Hershel M. Farkas, *Riemann surfaces*, Springer, 1992.
15. Hildebrandt, Klaus, Polthier, Konrad, Wardetzky, and Max, *On the convergence of metric and geometric properties of polyhedral surfaces*, *Geometriae Dedicata* **123** (2006), no. 1, 89–112.
16. L. Kantorovich, *On the translocation of masses*, C.R. (Dokl.) Acad. Sci. URSS (N.S.) **37** (1942), 199–201.
17. M.D. Plummer L. Lovász, *Matching theory*, North-Holland, 1986.
18. Parsons LM Liotti M Freitas CS Rainey L Kochunov PV Nickerson D Mikiten SA Fox PT Lancaster JL, Woldorff MG, *Automated talairach atlas labels for functional brain mapping*, *Human Brain Mapping* **10** (2000), 120–131.
19. Yaron Lipman and Ingrid Daubechies, *Comparing surfaces in polynomial time*, Submitted (2010).
20. ———, *Surface comparison with mass transportation*, Technical report, Princeton University (2010).
21. Yaron Lipman and Thomas Funkhouser, *Mobius voting for surface correspondence*, *ACM Transactions on Graphics (Proc. SIGGRAPH)* **28** (2009), no. 3.
22. Facundo Memoli, *On the use of gromov-hausdorff distances for shape comparison*, *Symposium on Point Based Graphics* (2007).
23. Facundo Mémoli and Guillermo Sapiro, *A theoretical and computational framework for isometry invariant recognition of point cloud data*, *Found. Comput. Math.* **5** (2005), no. 3, 313–347.
24. Billingsley Patrick, *Convergence of probability measures*, John Wiley & Sons, 1968.
25. Ulrich Pinkall and Konrad Polthier, *Computing discrete minimal surfaces and their conjugates*, *Experimental Mathematics* **2** (1993), 15–36.
26. Konrad Polthier, *Conjugate harmonic maps and minimal surfaces*, Preprint No. 446, TU-Berlin, SFB 288 (2000).
27. ———, *Computational aspects of discrete minimal surfaces*, *Global Theory of Minimal Surfaces*, Proc. of the Clay Mathematics Institute 2001 Summer School, David Hoffman (Ed.), CMI/AMS (2005).
28. Y. Rubner, C. Tomasi, and L. J. Guibas, *The earth mover’s distance as a metric for image retrieval*, *International Journal of Computer Vision* **40** (2000), no. 2, 99–121.
29. Conroy B Bryan RE Ramadge PJ Haxby JV Sabuncu MR, Singer BD, *Function-based intersubject alignment of human cortical anatomy*, *Cereb Cortex.* (2009).
30. Alexander Schrijver, *A course in combinatorial optimization, course note*, 2008.
31. George Springer, *Introduction to riemann surfaces*, AMS Chelsea Publishing, 1981.
32. Cedric Villani, *Topics in optimal transportation (graduate studies in mathematics, vol. 58)*, American Mathematical Society, March 2003.
33. W. Zeng, X. Yin, Y. Zeng, Y. Lai, X. Gu, and D. Samaras, *3d face matching and registration based on hyperbolic ricci flow*, *CVPR Workshop on 3D Face Processing* (2008), 1–8.
34. W. Zeng, Y. Zeng, Y. Wang, X. Yin, X. Gu, and D. Samaras, *3d non-rigid surface matching and registration based on holomorphic differentials*, *The 10th European Conference on Computer Vision (ECCV)* (2008).

APPENDIX A.

We prove Theorem 2.1. We start with a simple lemma showing that all Möbius transformations restricted to $\Omega_{0,R}$, $R < \infty$, are Lipschitz with a universal constant, for which we provide an upper bound.

Lemma A.1. *A Möbius transformation $m \in M_D$ restricted to $\Omega_{0,R}$, $R < \infty$ is Lipschitz continuous with Lipschitz constant $C_m \leq \frac{1-|a|^2}{(1-r_R|a|)^2}$, where $a = m^{-1}(0)$.*

Proof. Denote $m(z) = e^{i\theta} \frac{z-a}{1-z\bar{a}}$. Then, for $z, w \in \Omega_{0,R}$ we have

$$\begin{aligned} |m(z) - m(w)| &\leq \left| e^{i\theta} \frac{z-a}{1-z\bar{a}} - e^{i\theta} \frac{w-a}{1-w\bar{a}} \right| \leq \left| \frac{(z-a)(1-w\bar{a}) - (w-a)(1-z\bar{a})}{(1-z\bar{a})(1-w\bar{a})} \right| \\ &\leq \left| \frac{(z-w)(1-|a|^2)}{(1-z\bar{a})(1-w\bar{a})} \right| \leq |z-w| \frac{1-|a|^2}{(1-r_R|a|)^2}. \end{aligned}$$

□

Next we prove:

Theorem 2.1 *For continuously differentiable μ, ν ,*

$$\left| d_{\mu, \nu}^R(z_i, w_j) - \min_{m(z_i)=w_j} \sum_k \alpha_k |\mu(\tilde{m}_i(p_k)) - \nu(m(\tilde{m}_i(p_k)))| \right| \leq C \varphi(\{p_k\}),$$

where the constant C depends only on μ, ν, R .

Proof. First, denote $f(z) = \left| \mu(\tilde{m}_i(z)) - \nu(m(\tilde{m}_i(z))) \right|$. Then,

$$(A.1) \quad \left| \int_{\Omega_0} f(z) d\text{vol}_H(z) - \min_{m(z_i)=w_j} \sum_k \alpha_k f(p_k) \right| \leq \sum_k \int_{\Omega_0} |f(z) - f(p_k)| d\text{vol}_H(z) \\ \leq \omega_f^{\Omega_0}(\varphi(\{p_k\})) \int_{\Omega_0} d\text{vol}_H,$$

where the modulus of continuity $\omega_f^{\Omega_0}(h) = \sup_{|z-w|<h; z, w \in \Omega_0} |f(z) - f(w)|$ is used. Note that

$$(A.2) \quad \omega_f^{\Omega_0} \leq \omega_{\mu \circ \tilde{m}_i}^{\Omega_0} + \omega_{\nu \circ m \circ \tilde{m}_i}^{\Omega_0}.$$

Since μ, ν have continuous derivatives on compact domain, they are Lipschitz continuous. Denote their Lipschitz constants by C_μ, C_ν , respectively. From Lemma A.1 we see that, for $z, w \in \Omega_0$,

$$\left| \mu(\tilde{m}_i(z)) - \mu(\tilde{m}_i(w)) \right| \leq C_\mu \left| \tilde{m}_i(z) - \tilde{m}_i(w) \right| \leq C_\mu \frac{1 - |a|^2}{(1 - r_R|a|)^2} |z - w| \leq C_\mu \frac{1}{(1 - r_R)^2} |z - w|,$$

which is independent of \tilde{m}_i . Similarly,

$$\left| \nu(m(\tilde{m}_i(z))) - \nu(m(\tilde{m}_i(w))) \right| \leq C_\nu \left| m(\tilde{m}_i(z)) - m(\tilde{m}_i(w)) \right| \leq C_\nu \frac{1}{(1 - r_R)^2} |z - w|,$$

which is independent of m, \tilde{m}_i . Combining these with eq. (A.1-A.2) we get

$$\left| \int_{\Omega_0} f(z) d\text{vol}_H(z) - \min_{m(z_i)=w_j} \sum_k \alpha_k f(p_k) \right| \leq (C_\mu + C_\nu) \frac{\int_{\Omega_0} d\text{vol}_H}{(1 - r_R)^2} \varphi(\{p_k\}),$$

which finishes the proof. \square

APPENDIX B.

In this appendix we provide a short exposition on discrete and conjugate discrete harmonic functions on triangular meshes as presented in [7, 25, 26, 27], and we show how this theory can be used in our context to conformally flatten disk-type (or even just simply connected) triangular meshes.

We will use the same notations as in Section 2. Discrete harmonic functions are defined using a variational principle in the space of continuous piecewise linear functions defined over the mesh PL_M ([7]), as follows. Let us denote by $\phi_i(z)$, $i = 1, \dots, m$, the scalar functions that satisfy $\phi_j(v_i) = \delta_{i,j}$ and are linear on each triangle $f_{i,j,k} \in F$. Then, the (linear) space of continuous piecewise-linear function on M can be written in this basis:

$$PL_M = \left\{ \sum_{i=1}^m u_i \phi_i(z) \mid (u_1, \dots, u_m)^T \in \mathbb{R}^m \right\}.$$

Next, the following quadratic form is defined over PL_M :

$$(B.1) \quad E_{Dir}(u) = \sum_{f \in F} \int_f \langle \nabla u, \nabla u \rangle d\text{vol}_{\mathbb{R}^3},$$

where $\langle \cdot \rangle = \langle \cdot \rangle_{\mathbb{R}^3}$ denotes the inner-product induced by the ambient Euclidean space, and $d\text{vol}_{\mathbb{R}^3}$ is the induced volume element on f . This quadratic functional, the *Dirichlet energy*, can be written in coordinates of the basis defined earlier as follows:

$$(B.2) \quad E_{Dir} \left(\sum_i u_i \phi_i \right) = \sum_{i,j=1}^m u_i u_j \left[\sum_{f \in F} \int_f \langle \nabla \phi_i, \nabla \phi_j \rangle \right] d\text{vol}_{\mathbb{R}^3} = \sum_{i,j=1}^m u_i u_j \int_M \langle \nabla \phi_i, \nabla \phi_j \rangle d\text{vol}_{\mathbb{R}^3}.$$

The discrete harmonic functions are then defined as the functions $u \in PL_M$ that are critical for $E_{Dir}(u)$, subject to some constraints on the boundary of M . The linear equations for discrete harmonic function

$u \in PL_M$ are derived by partial derivatives of E_{Dir} , (B.2) w.r.t. $u_i, i = 1, \dots, m$:

$$(B.3) \quad \frac{\partial E_{Dir}(u)}{\partial u_k} = 2 \sum_{i=1}^m u_i \left[\sum_{f \in F} \int_f \langle \nabla \phi_i, \nabla \phi_k \rangle \right] d\text{vol}_{\mathbb{R}^3} = 2 \int_M \langle \nabla u, \nabla \phi_k \rangle d\text{vol}_{\mathbb{R}^3} = 2 \int_{R_k} \langle \nabla u, \nabla \phi_k \rangle d\text{vol}_{\mathbb{R}^3},$$

where $R_k \subset M$ is the 1-ring neighborhood of vertex v_k . The last equality uses that ϕ_k is supported on R_k .

Now, let $u = \sum_i u_i \phi_i$ be a discrete harmonic function. Pinkall and Polthier observed that conjugating the piecewise-constant gradient field ∇u (constant on each triangle $f \in F$), i.e. rotating the gradient ∇u in each triangle f by $\pi/2$ in the positive (= counterclockwise) sense (we assume M is orientable), results in a new vector field $*du = Jdu$ with the special property that its integrals along (closed) paths that cross edges only at their mid-points are systematically zero (see for example [27]). This means in particular that we can define a piecewise linear function $*u$ such that its gradient satisfies $d*u = *du$ and that is furthermore continuous through the mid-edges $\mathbf{v} \in \mathbf{V}$. The space of piecewise-linear functions on meshes that are continuous through the mid-edges is well-known in the finite-element literature, where it is called $ncPL_M$, the space of non-conforming finite elements [3]. The Dirichlet form (B.1) is defined over the space of non-conforming elements $ncPL_M$ as well; the non-conforming discrete harmonic functions are defined to be the functions $v \in ncPL_M$ that are critical for E_{Dir} and that satisfy some constraints on the mid-edges of the boundary of the mesh. Polthier [27] shows that if $u \in PL_M$ is a discrete harmonic function, then $*u \in ncPL_M$ is also discrete harmonic, with the same Dirichlet energy, and vice-versa. Solving for the discrete harmonic function after fixing values at the boundaries amounts to solving a sparse linear system which is explicitly given in [27].

This theory can be used to define discrete conformal mappings, and used to flatten a mesh in a “discrete conformal” manner, as follows. The flattening is done by constructing a pair of conjugate piecewise linear functions $(u, *u)$ where $u \in PL_M, *u \in ncPL_M$, and the flattening map $\Phi : \mathbf{M} \rightarrow \mathbb{C}$ is given by

$$(B.4) \quad \Phi = u + i * u.$$

Since $d*u = Jdu$, Φ is a similarity transformation on each triangle $f \in F$. Furthermore, Φ is continuous through the mid-edges $\mathbf{v}_r \in \mathbf{V}$. This means that Φ is well-defined on the mid-edges \mathbf{V} and maps them to the complex plane.

The function u is defined by choosing an arbitrary triangle $f_{out} \in F$, excising it from the mesh, setting the values of u at two of f_{out} 's vertices u_{i_1}, u_{i_2} to 0 and 1, respectively, and then solving for the discrete harmonic u that satisfies these constraints. See for example Figure 2 (top-left); the “missing mid-edge face” corresponding to the excised face f_{out} would have connected the three mid-edge vertices that have a only one mid-edge face touching them. The conjugate function $*u$ is constructed by a simple conjugation (and integration) process as described in [27] and [21].

A surprising property of the Discrete Uniformization Φ as it is defined above, which nicely imitates the continuous theory (see [31]) is that it takes the boundaries of \mathcal{M} to horizontal slits, see Figure 2, top row (boundary vertices colored in red). This property allows us to easily construct a closed form analytic map (with “analytic” in its standard complex analytic sense) that will further bijectively map the entire complex plane \mathbb{C} minus the slit to the open unit disk, completing our Uniformization procedure.

This property is proved by arguments similar to those for Proposition 35 in [27]; see also [21]. More precisely, we have

Theorem B.1. *Let $\Phi : \mathbf{M} \rightarrow \mathbb{C}$ be the flattening map from the mid-edge mesh \mathbf{M} of a mesh \mathcal{M} with boundary, using a discrete harmonic and conjugate harmonic pair as described above. Then, for each connected component of the boundary of \mathcal{M} , the mid-edge vertices of boundary edges are all mapped onto one line segment parallel to the real axis.*

Proof. Suppose $u = \sum_i u_i \phi_i(\cdot)$ is a discrete harmonic, piecewise linear and continuous function, defined at each vertex $v_i \in V$, excluding the two vertices of the excised triangle for which values are prescribed; then

we have, by (B.3),

$$(B.5) \quad \int_{R_i} \langle \nabla \phi_i, \nabla u \rangle d\text{vol}_{\mathbb{R}^3} = 0,$$

Next, consider a boundary vertex v_j of the mesh \mathcal{M} . Denote by $\mathbf{v}_r, \mathbf{v}_s$ the mid-edge vertices on the two boundary edges touching vertex v_j . We will show that $*u(\mathbf{v}_r) = *u(\mathbf{v}_s)$; this will imply the theorem, since $*u$ gives the imaginary coordinate for the images of the mid-edge vertices under the flattening map (see (B.4)).

Observe that on the triangle $f_{i,j,k}$,

$$(B.6) \quad \nabla \phi_j = \frac{J(v_i - v_k)}{2 \text{vol}_{\mathbb{R}^3}(f_{i,j,k})}.$$

Recalling that $\nabla *u = J\nabla u$, using (B.6), and $J^T = -J$, we obtain

$$\begin{aligned} *u(\mathbf{v}_r) - *u(\mathbf{v}_s) &= \int_{\gamma} d *u = \int_{\gamma} *du = \sum_{f_{i,j,k} \ni v_j} \left\langle J\nabla u |_{f_{i,j,k}}, \frac{1}{2}(v_i - v_k) \right\rangle \\ &= \sum_{f_{i,j,k} \ni v_j} \left\langle \nabla u |_{f_{i,j,k}}, \frac{1}{2}J^T(v_i - v_k) \right\rangle \\ &= \sum_{f_{i,j,k} \ni v_j} \langle \nabla u |_{f_{i,j,k}}, -\nabla \phi_j |_f \rangle \text{vol}_{\mathbb{R}^3}(f) \\ &= - \int_M \langle \nabla u, \nabla \phi_j \rangle d\text{vol}_{\mathbb{R}^3} \\ &= 0, \end{aligned}$$

where γ is the piecewise linear path starting at \mathbf{v}_r and passing through the mid-edge vertices of the 1-ring neighborhood of v_j ending at \mathbf{v}_s . The last equality is due to (B.3). \square

A natural question, when dealing with any type of finite-element approximation, concerns convergence as the mesh is refined: convergence in what sense, and at what rate? For discrete harmonic functions over meshes, this convergence is discussed in [15, 26]. Note that these convergence results are in the weak sense; this motivated our defining the discrete conformal factors $\mu_{\mathbf{f}}$ via integrated quantities (volumes) in Section 2.

Finally, we note that the method presented here for Discrete Uniformization is just one option among several; other authors have suggested other techniques; for example [12]. Typically, this part of the complete algorithm described in this paper could be viewed as a “black box”: the remainder of the algorithm would not change if one method of Discrete Uniformization is replaced by another.

APPENDIX C.

In this Appendix we prove a lemma used in the proof of Theorem 2.4.

Lemma *The $N \times N$ matrices π satisfying*

$$(C.1) \quad \left\{ \begin{array}{l} \sum_i \pi_{ij} \leq 1 \\ \sum_j \pi_{ij} \leq 1 \\ \pi_{ij} \geq 0 \\ \sum_{i,j} \pi_{ij} = M < N \end{array} \right.$$

constitute a convex polytope \mathcal{P} of which the extremal points are exactly those π that satisfy all these constraints, and that have all entries equal to either 0 or 1.

Remark. Note that the matrices $\pi \in \mathcal{P}$ with all entries in $\{0, 1\}$ have exactly M entries equal to 1, and all other entries equal to zero; if one removes from these matrices all rows and columns that consist of only zeros, what remains is a $M \times M$ permutation matrix.

Proof. \mathcal{P} can be considered as a subset of \mathbb{R}^{N^2} , with all entries nonnegative, summing to M . The two inequalities in (C.1) imply that the entries of any $\pi \in \mathcal{P}$ are bounded by 1. These inequalities can also be rewritten as the constraint that every entry of $A\mathcal{P} - b \in \mathbb{R}^{2N}$ is non positive, where A is a $\mathbb{R}^{2N} \times \mathbb{R}^{N^2}$ matrix, and b is a vector in \mathbb{R}^{2N} . It follows that \mathcal{P} is a (bounded) convex polytope in \mathbb{R}^{N^2} .

If $\pi \in \mathcal{P} \subset \mathbb{R}^{N^2}$ has entries equal to only 0 or 1, then π must be an extremal point of \mathcal{P} by the following argument. If $\pi_\ell = 1$, and π is a nontrivial convex combination of π^1 and π^2 in \mathcal{P} , then

$$\pi = \lambda \pi^1 + (1 - \lambda) \pi^2 \text{ with } \lambda \in (0, 1) \implies 1 = \lambda \pi_\ell^1 + (1 - \lambda) \pi_\ell^2 \text{ with } \pi_\ell^1, \pi_\ell^2 \geq 0 \implies \pi_\ell^1 = \pi_\ell^2 = 1.$$

A similar argument can be applied for the entries of π that are 0. It follows that we must have $\pi^1 = \pi = \pi^2$, proving that π is extremal.

It remains thus to prove only that \mathcal{P} has no other extremal points. To achieve this, it suffices to prove that the extremal points of \mathcal{P} are all integer vectors, i.e. vectors all entries of which are integers – once this is established, the Lemma is proved, since the only integer vectors in \mathcal{P} are those with all entries in $\{0, 1\}$.

To prove that the extremal points of \mathcal{P} are all integer vectors, we invoke the Hoffman-Kruskal theorem (see [17], Theorem 7C.1), which states that, given a $L \times K$ matrix \mathbb{M} , with all entries in $\{-1, 0, 1\}$, and a vector $b \in \mathbb{R}^L$ with integer entries, the vertices of the polytope defined by $\{x \in \mathbb{R}^K; (\mathbb{M}x)_\ell \leq b_\ell \text{ for } \ell = 1, \dots, L\}$ are all integer vectors in \mathbb{R}^K if and only if the matrix \mathbb{M} is totally unimodular, i.e. if and only if every square submatrix of \mathbb{M} has determinant 1, 0 or -1 .

We first note that (C.1) can indeed be written in this special form. The equality $\sum_{i,j} \pi_{ij} = M$ can be recast as the two inequalities $\sum_{i,j} \pi_{ij} \leq M$ and $-\sum_{i,j} \pi_{ij} \leq -M$. The full system (C.1) can then be written as $(\mathbb{M}\pi)_\ell \leq b_\ell$ for $\ell = 1, \dots, L$, where \mathbb{M} is a $(2N + 2 + N^2) \times N^2$ matrix constructed as follows. Its first $2N$ rows correspond to the constraints on the sums over rows and columns; the entries of the next row are all 1, and of the row after that, all -1 – these two rows correspond to the constraint $\sum_{i,j} \pi_{ij} = M$; the final $N^2 \times N^2$ block is diagonal, with all its diagonal entries equal to -1 . The first $2N$ entries of b are 1; the next 2 entries are M and $-M$; its final N^2 entries are 0. By the Hoffman-Kruskal theorem it suffices thus to show that \mathbb{M} is totally unimodular.

Because the last N^2 rows, the *bottom rows* of \mathbb{M} , have only one non-zero entry, which equals -1 , we can disregard them. Indeed, if we take a square submatrix of \mathbb{M} that includes (part of) one of these bottom rows, then the determinant of the submatrix is 0 if only zero entries of the bottom row ended up in the submatrix; if the one -1 entry of the bottom row is an entry in the submatrix, then the determinant is, possibly up to a sign change, the same as if that row and the column of the -1 entry are removed. By this argument, we can remove all the rows of the submatrix partaking of the bottom rows of \mathbb{M} .

We thus have to check unimodularity only for \mathbb{M}' , the submatrix of \mathbb{M} given by its first $2N + 2$ rows. If any submatrix contains (parts of) both the $(2N + 1)$ st and the $(2N + 2)$ nd row, then the determinant is automatically zero, since the second of these two rows equals the first one, multiplied by -1 . This reduces the problem to checking that \mathbb{M}'' , the submatrix of \mathbb{M} given by its first $2N + 1$ rows, is totally unimodular.

We now examine the top $2N$ rows of \mathbb{M}'' more closely. A little scrutiny reveals that it is, in fact, the adjacency matrix \mathbb{G} of the complete bipartite graph with N vertices in each part.¹ It is well-known (see e.g. Theorem 8.3 in [30]) that this adjacency matrix is totally unimodular, so any square submatrix of \mathbb{M}'' that does not

¹ The adjacency matrix A for a graph \mathcal{G} has as many columns as \mathcal{G} has edges, and as many rows as \mathcal{G} has vertices; if we label the rows and columns of A accordingly, then $A_{ve} = 1$ if the vertex v is an end point of the edge e ; otherwise $A_{ve} = 0$. An adjacency matrix thus has exactly two nonzero entries (both equal to 1) in each column. The number of nonzero entries in the row with index v is the degree of v in the graph.

involve the $(2N + 1)$ st row of \mathbb{M}'' is already known to have determinant 0, 1 or -1 . We thus have to check only submatrices that involve the last row, i.e. matrices that consist of a $(n - 1) \times n$ submatrix of \mathbb{G} , with an added n th row with all entries equal to 1. We'll denote such submatrices by \mathbb{G}' .

We can then use a simple induction argument on n to finish the proof. The case $n = 2$ is trivial. In proving the induction step for $n = m$, we can assume that each of the top $m - 1$ rows of our $m \times m$ submatrix \mathbb{G}' contains at least two entries equal to 1, since otherwise the determinant of \mathbb{G}' would automatically be 0, 1 or -1 by induction.

The first $m - 1$ rows of \mathbb{G}' correspond to vertices in the bipartite graph, and can thus be partitioned into two sets S_1 and S_2 , based on which of the two parts of N vertices in the graph they pertain to. Let us call S the larger of S_1 and S_2 ; S consists of at least $\lceil \frac{m-1}{2} \rceil$ rows. Let us examine the $(\#S) \times m$ sub-matrix \mathbb{G}'' constructed from exactly these rows. We know that each column of \mathbb{G}'' has exactly one entry 1, since all the rows of \mathbb{G}'' correspond to the same group of vertices in the bipartite graph. Therefore, summing all the rows of \mathbb{G}'' gives a vector v of only zeros and ones; since each row in \mathbb{G}'' contains at least two entries equal to 1, the sum of all entries in v is at least $2 \lceil \frac{m-1}{2} \rceil \geq m - 1$. The vector v has thus at least $m - 1$ entries equal to 1; the remaining m th entry of this linear combination of the top $m - 1$ rows of \mathbb{G}' is either 1 or 0. In the first case, the determinant of \mathbb{G}' vanishes, since its last row also consists of only ones. In the second case, we can subtract v from the last row of \mathbb{G}' without changing the value of the determinant; the resulting last row has all entries but one equal to 0, with a remaining entry equal to 1. The determinant is then given by the minor of this remaining entry, and is thus 0, 1 or -1 by the unimodularity of \mathbb{G} . \square

APPENDIX D.

In this Appendix we provide a constructive procedure and convergence analysis for approximating the optimal transport cost between *general* separable complete compact metric spaces $(\mathcal{X}, d_{\mathcal{X}}), (\mathcal{Y}, d_{\mathcal{Y}})$ each equipped with a probability measure $\mu \in P(\mathcal{X}), \nu \in P(\mathcal{Y})$, where $P(\mathcal{X})$ ($P(\mathcal{Y})$) denotes the set of probability measures on \mathcal{X} (\mathcal{Y}). In the context of the algorithm previously described \mathcal{X}, \mathcal{Y} are the two given surfaces, $d_{\mathcal{X}}, d_{\mathcal{Y}}$ the corresponding geodesic distance metric functions, and μ, ν the volume element of the surfaces induced from the metric tensors, respectively. (note, that previously we denoted these by $\tilde{\mu}, \tilde{\nu}$.) Since R, μ, ν are kept fixed through this discussion, we will denote, for brevity, $c(x, y) = d_{\mu, \nu}^R(x, y)$.

The Kantorovich optimal transportation cost of the measures μ, ν is defined as

$$(D.1) \quad T_c(\mu, \nu) = \inf_{\pi \in \Pi(\mu, \nu)} \int_{\mathcal{X} \times \mathcal{Y}} c(x, y) d\pi(x, y),$$

where $\Pi(\mu, \nu) \subset P(\mathcal{X} \times \mathcal{Y})$ is the set of probability measures on $\mathcal{X} \times \mathcal{Y}$ with marginals μ, ν , that is, $\pi \in \Pi(\mu, \nu) \Rightarrow \pi(A \times \mathcal{Y}) = \mu(A)$ and $\pi(\mathcal{X} \times A') = \nu(A')$, for all Borel $A \subset \mathcal{X}, A' \subset \mathcal{Y}$.

The main goal of this section is to present an *approximation result* for $T_c(\mu, \nu)$ in this general framework. In particular, this result will assure the convergence of our algorithm.

To our knowledge, the only related result talks merely about convergence of the optimal cost (e.g., [32], Theorem 5.20). However, for practical applications it is important to control the *rate* of convergence, and therefore to be able to compute error-bounded approximations.

In the specific case of $c(x, y) = \|x - y\|^2$ there are good approximation techniques that rely on the polar decomposition of Brenier, for example the work of Haker and collaborators [13]. However, as far as we are aware no approximation result is known in the general metric case as required here.

We will show that solving discrete mass-transportation between two sets of discrete measures μ_S, ν_T , based on Voronoi diagrams of two collections of points $S = \{s_i\} \subset \mathcal{X}, T = \{t_j\} \subset \mathcal{Y}$, achieve linear approximation order to the continuous limit mass-transport cost $T_c(\mu, \nu)$:

$$\left| T_c(\mu, \nu) - T_c(\mu_S, \nu_T) \right| \leq \omega_c(2h),$$

where $\omega_c(\alpha)$ is the modulus of continuity of c defined by

$$\omega_c(\alpha) = \sup_{d_{\mathcal{X}}(x,x') + d_{\mathcal{Y}}(y,y') < \alpha} |c(x,y) - c(x',y')|,$$

and $h = \max\{\eta(S), \eta(T)\}$, where the *fill distances* $\eta(S), \eta(T)$ are defined by

$$(D.2) \quad \eta(S) = \sup \left\{ r \in \mathbb{R} \mid \exists x \in \mathcal{X} \text{ s.t. } B(x, r) \cap S = \emptyset \right\},$$

where $B(x, r) = \{q \in \mathcal{X} \mid d_{\mathcal{X}}(x, q) < r\}$ (and similarly for $\eta(T)$). Intuitively, the fill distance $\eta(S)$ of a point set S is the radius of the largest open ball that can be plugged into the space without containing any point of S .

In particular, for Lipschitz cost function c with Lipschitz constant λ , we have the following bound for the error in the approximation:

$$(D.3) \quad \left| T_c(\mu, \nu) - T_c(\mu_S, \nu_T) \right| \leq 2\lambda h.$$

In turn, this result suggests an algorithm for approximating $T_c(\mu, \nu)$: simply spread points $S \subset \mathcal{X}$ and $T \subset \mathcal{Y}$ such that no big empty space is left uncovered, then compute $T_c(\mu_S, \nu_T)$ using linear-programming solver.

D.1. Voronoi cells and discrete measures. Let $(\mathcal{X}, d_{\mathcal{X}}, \mu), (\mathcal{Y}, d_{\mathcal{Y}}, \nu)$ be two compact, complete, separable metric spaces with probability measures defined over the Borel sets.

The discrete measures will be based on discrete sets of points $S = \{s_i\}_{i=1}^m \subset \mathcal{X}, T = \{t_i\}_{i=1}^n \subset \mathcal{Y}$ and the coarseness of the sets will be measured by means of the so-called *fill-distance* $\eta(S), \eta(T)$ of the sets S, T . The fill-distance of $S \subset \mathcal{X}$ is defined in eq. (D.2). The sets get “finer” as $\max\{\eta(S), \eta(T)\} \rightarrow 0$.

For set of points $S = \{s_i\}_{i=1}^m \subset \mathcal{X}$ we define

$$(D.4) \quad O_i^S = \left\{ x \in \mathcal{X} \mid d_{\mathcal{X}}(x, s_i) < \min_{j \neq i} d_{\mathcal{X}}(x, s_j) \right\}.$$

$$(D.5) \quad C_i^S = \left\{ x \in \mathcal{X} \mid d_{\mathcal{X}}(x, s_i) \leq \min_{j \neq i} d_{\mathcal{X}}(x, s_j) \right\}.$$

Then, Voronoi cells for the point set S is any collection of sets $\{V_i\}_{i=1}^m$ satisfying

- (1) $\cup_{i=1}^m V_i = \mathcal{X}$.
- (2) $V_i \cap V_j = \emptyset$ for $i \neq j$.
- (3) $O_i^S \subset V_i \subset C_i^S$, for all $i = 1, \dots, m$.

We will prove now a simple lemma, for later use, connecting the fill-distance with the geometry of the Voronoi cells.

Lemma D.1. *Let $S = \{s_i\}_{i=1}^m \subset \mathcal{X}$. If $\{V_i\}_{i=1}^m$ is a collection of Voronoi cells corresponding to S , then for all $\varepsilon > 0$,*

$$V_i \subset B(s_i, \eta(S) + \varepsilon), \quad i = 1, \dots, m$$

Proof. Take $x \notin B(s_i, \eta(S) + \varepsilon)$.

By the definition of the fill-distance we have that

$$B\left(x, \eta(S) + \frac{\varepsilon}{2}\right) \cap S \neq \emptyset.$$

That is, there exists $s_k \in S, k \neq i$, such that

$$d_{\mathcal{X}}(x, s_k) < \eta(S) + \frac{\varepsilon}{2}.$$

However,

$$d_{\mathcal{X}}(x, s_i) \geq \eta(S) + \varepsilon > d_{\mathcal{X}}(x, s_k).$$

Hence from the definition of the Voronoi cells

$$x \in \mathcal{X} \setminus C_i^S \subset \mathcal{X} \setminus V_i,$$

that is $x \notin V_i$. □

Given a set of points and a Voronoi cell collection $S, \{V_i\}_{i=1}^m$ we define a discrete measure μ_S by

$$(D.6) \quad \mu_S = \sum_{i=1}^m \mu(V_i) \delta_{s_i},$$

where δ_{s_i} is the dirac measure centered at s_i . That is

$$\int_{\mathcal{X}} f d\mu_S = \sum_{i=1}^m \mu(V_i) f(s_i).$$

Similarly we define Voronoi cell collection $\{W_j\}_{j=1}^n$ for point set $T \subset \mathcal{Y}$, and corresponding discrete measure ν_T .

Let us prove that the discrete measures μ_S, ν_T converge in the weak sense to μ, ν . By weak convergence $\mu_S \rightarrow \mu$ of measure we mean (see for example [24]) that for every continuous bounded function $f : \mathcal{X} \rightarrow \mathbb{R}$ there exists

$$\int_{\mathcal{X}} f d\mu_S \rightarrow \int_{\mathcal{X}} f d\mu, \quad \text{as } \eta(S) \rightarrow 0.$$

Theorem D.2. $\lim_{\eta(S) \rightarrow 0} \int_{\mathcal{X}} f d\mu_S = \int_{\mathcal{X}} f d\mu$, for all $f : \mathcal{X} \rightarrow \mathbb{R}$ bounded and continuous.

Proof. X is compact therefore f is uniformly continuous. Take arbitrary $\varepsilon > 0$, let $\delta(\varepsilon) > 0$ be such that

$$x, x' \in \mathcal{X}, d_{\mathcal{X}}(x, x') < \delta(\varepsilon) \Rightarrow |f(x) - f(x')| < \varepsilon.$$

For S with $\eta(S) < \delta(\varepsilon)$ we have

$$\begin{aligned} \left| \int_{\mathcal{X}} f d\mu - \int_{\mathcal{X}} f d\mu_S \right| &= \left| \sum_{i=1}^m \int_{V_i} (f(x) - f(s_i)) d\mu \right| \leq \\ &\leq \sum_{i=1}^m \int_{V_i} |f(x) - f(s_i)| d\mu \leq \sum_{i=1}^m \varepsilon \mu(V_i) = \varepsilon, \end{aligned}$$

where in the second to last transition we used the fact that $V_i \subset B(s_i, \delta(\varepsilon))$ which we know is the case from Lemma D.1. □

Lastly, we will denote by $\Pi(\mu_S, \nu_T) \subset P(S \times T)$ the subset of probability measures on the discrete product space $S \times T$ with marginals μ_S, ν_T .

D.2. Approximation of optimal cost. In this subsection we prove the main result of this appendix. Namely, that the optimal transport cost $T_c(\mu_S, \nu_T)$ of the discrete measures μ_S, ν_T is an ε -approximation to the optimal transport cost $T_c(\mu, \nu)$ of μ, ν if the fill-distance $h = \max\{\eta(S), \eta(T)\} < \frac{1}{2}\delta(\varepsilon)$, where $\delta(\varepsilon)$ is the uniform continuity constant of c .

Actually, we will prove a slightly stronger result: denote the sets

$$(D.7) \quad \mathcal{A} = \left\{ \int_{\mathcal{X} \times \mathcal{Y}} c d\pi \mid \pi \in \Pi(\mu, \nu) \right\}, \quad \mathcal{B} = \left\{ \int_{\mathcal{X} \times \mathcal{Y}} c d\pi \mid \pi \in \Pi(\mu_S, \nu_T) \right\}.$$

We will show that the Hausdorff distance $d_H(\mathcal{A}, \mathcal{B}) \rightarrow 0$ as $h \rightarrow 0$. Where by Hausdorff distance of two sets $\mathcal{A}, \mathcal{B} \subset \mathbb{R}$ we mean

$$d_H(\mathcal{A}, \mathcal{B}) = \inf \left\{ r \mid \mathcal{B} \subset U(\mathcal{A}, r), \mathcal{A} \subset U(\mathcal{B}, r) \right\},$$

where $U(\mathcal{A}, r) = \cup_{a \in \mathcal{A}} B(a, r)$ and $B(a, r)$ is the open ball of radius r centered at a . Moreover, as announced at the introduction we will provide a linear (in h) bound controlling the convergence rate, for Lipschitz cost function c .

Theorem D.3. *If $c : \mathcal{X} \times \mathcal{Y} \rightarrow \mathbb{R}_+$ is a continuous function, \mathcal{X}, \mathcal{Y} compact complete separable metric spaces. Let $h = \max\{\eta(S), \eta(T)\}$ then,*

$$d_H(\mathcal{A}, \mathcal{B}) \leq \omega_c(2h),$$

where \mathcal{A}, \mathcal{B} are defined in (D.7). In particular,

$$\left| T_c(\mu, \nu) - T_c(\mu_S, \nu_T) \right| \leq \omega_c(2h).$$

Proof. Take arbitrary $S = \{s_i\}_{i=1}^m \subset \mathcal{X}$, $T = \{t_i\}_{i=1}^n \subset \mathcal{Y}$. Choose collections of Voronoi cells $\{V_i\}_{i=1}^m$, $\{W_j\}_{j=1}^n$ for S, T respectively.

Now take $\pi \in \Pi(\mu, \nu)$.

Set

$$\Lambda = \sum_{i=1}^m \sum_{j=1}^n \pi(V_i \times W_j) \delta_{s_i, t_j}.$$

Then,

$$\begin{aligned} \Lambda(A \times \mathcal{Y}) &= \sum_{i=1}^m \sum_{j=1}^n \pi(V_i \times W_j) \delta_{s_i}(A) = \\ &= \sum_{i=1}^m \pi(V_i \times \mathcal{Y}) \delta_{s_i}(A) = \sum_{i=1}^m \mu(V_i) \delta_{s_i}(A) = \mu_S(A). \end{aligned}$$

Similarly

$$\Lambda(\mathcal{X} \times A') = \nu_T(A').$$

Therefore

$$\Lambda \in \Pi(\mu_S, \nu_T).$$

Moreover,

$$\begin{aligned} \left| \int_{\mathcal{X} \times \mathcal{Y}} c \, d\pi - \int_{\mathcal{X} \times \mathcal{Y}} c \, d\Lambda \right| &= \left| \sum_{i=1}^m \sum_{j=1}^n \int_{V_i \times W_j} [c(x, y) - c(s_i, t_j)] \, d\pi \right| \leq \\ &= \sum_{i=1}^m \sum_{j=1}^n \int_{V_i \times W_j} |c(x, y) - c(s_i, t_j)| \, d\pi. \end{aligned}$$

For $(x, y) \in V_i \times W_j$, we have $d_{\mathcal{X}}(x, s_i) \leq \eta(S)$, $d_{\mathcal{Y}}(y, t_j) \leq \eta(T)$ which implies

$$(D.8) \quad |c(x, y) - c(s_i, t_j)| \leq \omega_c(\eta(S) + \eta(T)) \leq \omega_c(2h).$$

So we have

$$\left| \int_{\mathcal{X} \times \mathcal{Y}} c \, d\pi - \int_{\mathcal{X} \times \mathcal{Y}} c \, d\Lambda \right| \leq \omega_c(2h) \sum_{i=1}^m \sum_{j=1}^n \pi(V_i \times W_j) = \omega_c(2h),$$

since $\{V_i \times W_j\}_{i,j=1,1}^{n,m}$ form a partition of $X \times Y$. So we proved that

$$\mathcal{A} \subset \overline{U(\mathcal{B}, \omega_c(2h))}.$$

We now prove the other direction. Take $\Lambda \in \Pi(\mu_S, \nu_T)$.

Denote by $\mu \times \nu|_{V_i \times W_j}$ the product measure $\mu \times \nu$ restricted to $V_i \times W_j \subset \mathcal{X} \times \mathcal{Y}$.

That is,

$$\mu \times \nu|_{V_i \times W_j}(A \times A') = \mu \times \nu((V_i \times W_j) \cap (A \times A')) = \mu(V_i \cap A) \nu(W_j \cap A').$$

Now pick

$$\pi = \sum_{i=1}^m \sum_{j=1}^n \frac{\Lambda(V_i \times W_j)}{\mu(V_i)\nu(W_j)} \mu \times \nu|_{V_i \times W_j}.$$

Then,

$$\begin{aligned} \pi(A \times \mathcal{Y}) &= \sum_{i=1}^m \sum_{j=1}^n \frac{\Lambda(V_i \times W_j)}{\mu(V_i)\nu(W_j)} \mu(V_i \cap A) \nu(W_j \cap \mathcal{Y}) = \\ &= \sum_{i=1}^m \sum_{j=1}^n \frac{\Lambda(V_i \times W_j)}{\mu(V_i)} \mu(V_i \cap A) = \\ &= \sum_{i=1}^m \frac{\mu(V_i \cap A)}{\mu(V_i)} \left[\sum_{j=1}^n \Lambda(V_i \times W_j) \right] = \\ &= \sum_{i=1}^m \frac{\mu(V_i \cap A)}{\mu(V_i)} \Lambda(V_i \times \mathcal{Y}) = \\ &= \sum_{i=1}^m \frac{\mu(V_i \cap A)}{\mu(V_i)} \mu(V_i) = \\ &= \sum_{i=1}^m \mu(V_i \cap A) = \mu(\mathcal{X} \cap A) = \mu(A). \end{aligned}$$

Similarly

$$\pi(\mathcal{X} \times A') = \nu(A').$$

Therefore,

$$\pi \in \Pi(\mu, \nu).$$

Now,

$$\begin{aligned} &\left| \int_{\mathcal{X} \times \mathcal{Y}} c \, d\pi - \int_{\mathcal{X} \times \mathcal{Y}} c \, d\Lambda \right| = \\ &\left| \sum_{i=1}^m \sum_{j=1}^n \frac{\Lambda(V_i \times W_j)}{\mu(V_i)\nu(W_j)} \int_{V_i \times W_j} c \, d(\mu \times \nu) - \sum_{i=1}^m \sum_{j=1}^n c(s_i, t_j) \Lambda(V_i \times W_j) \right| = \\ &\left| \sum_{i=1}^m \sum_{j=1}^n \left[\frac{\Lambda(V_i \times W_j)}{\mu(V_i)\nu(W_j)} \int_{V_i \times W_j} c \, d(\mu \times \nu) - \frac{\Lambda(V_i \times W_j)}{\mu(V_i)\nu(W_j)} \int_{V_i \times W_j} c(s_i, t_j) \, d(\mu \times \nu) \right] \right| \leq \\ &\sum_{i=1}^m \sum_{j=1}^n \frac{\Lambda(V_i \times W_j)}{\mu(V_i)\nu(W_j)} \int_{V_i \times W_j} |c(x, y) - c(s_i, t_j)| \, d(\mu \times \nu). \end{aligned}$$

As before, for $(x, y) \in V_i \times W_j$, we have $d_{\mathcal{X}}(x, s_i) \leq \eta(S)$, $d_{\mathcal{Y}}(y, t_j) \leq \eta(T)$ therefore

$$|c(x, y) - c(s_i, t_j)| \leq \omega_c(\eta(S) + \eta(T)) \leq \omega_c(2h).$$

And therefore

$$\begin{aligned} \left| \int_{\mathcal{X} \times \mathcal{Y}} c \, d\pi - \int_{\mathcal{X} \times \mathcal{Y}} c \, d\Lambda \right| &\leq \omega_c(2h) \sum_{i=1}^m \sum_{j=1}^n \frac{\Lambda(V_i \times W_j)}{\mu(V_i)\nu(W_j)} \mu(V_i)\nu(W_j) = \\ &= \omega_c(2h) \sum_{i=1}^m \sum_{j=1}^n \Lambda(V_i \times W_j) = \omega_c(2h). \end{aligned}$$

So we proved

$$\mathcal{B} \subset \overline{U(\mathcal{A}, \omega_c(2h))},$$

and

$$d_H(\mathcal{A}, \mathcal{B}) \leq \omega_c(2h).$$

In particular this means that

$$\left| T_c(\mu, \nu) - T_c(\mu_S, \nu_T) \right| = \left| \inf(\mathcal{A}) - \inf(\mathcal{B}) \right| \leq \omega_c(2h).$$

□

We will call $c : \mathcal{X} \times \mathcal{Y} \rightarrow \mathbb{R}_+$ Lipschitz continuous with a constant λ if

$$|c(x, y) - c(x', y')| \leq \lambda(d_{\mathcal{X}}(x, x') + d_{\mathcal{Y}}(y, y')), \quad \forall x, x' \in \mathcal{X}, y, y' \in \mathcal{Y}.$$

Theorem D.4. *if c is uniformly continuous then*

$$T_c(\mu_S, \nu_T) \rightarrow T_c(\mu, \nu),$$

as $h \rightarrow 0$, and if c is Lipschitz continuous with a constant λ , then

$$|T_c(\mu, \nu) - T_c(\mu_S, \nu_T)| < 2\lambda h,$$

where, as before, $h = \max\{\eta(S), \eta(T)\}$.

Proof. The result follow from the fact that for uniformly continuous c , $\omega_c(t) \rightarrow 0$ as $t \rightarrow 0$, and that for Lipschitz c with constant λ , $\omega_c(t) \leq \lambda t$. □

Therefore, a simple generalization to the non-compact case, that is when \mathcal{X}, \mathcal{Y} are complete separable metric spaces, can be achieved by requiring that $c : \mathcal{X} \times \mathcal{Y} \rightarrow \mathbb{R}_+$ is uniformly continuous on $\mathcal{X} \times \mathcal{Y}$.

Corollary D.5. *For \mathcal{X}, \mathcal{Y} complete, separable metric spaces, and $c : \mathcal{X} \times \mathcal{Y} \rightarrow \mathbb{R}_+$ uniformly continuous*

$$T_c(\mu_S, \nu_T) \rightarrow T_c(\mu, \nu).$$

Moreover, for Lipschitz c with Lipschitz constant λ

$$|T_c(\mu, \nu) - T_c(\mu_S, \nu_T)| < 2\lambda h,$$

where, as before, $h = \max\{\eta(S), \eta(T)\}$.

Note that our argument used only one specific property of Voronoi cells, namely that each is contained in an h -size closed ball. Many other ways to partition \mathcal{X} and \mathcal{Y} can be considered. The next Lemma uses a well known property of the Voronoi cells to show that the proposed discretization with Voronoi cells is in some sense optimal.

Lemma D.6. *Let $c : \mathcal{X} \times \mathcal{Y} \rightarrow \mathbb{R}_+$ be Lipschitz with constant λ , and let $S = \{s_i\}_{i=1}^m \subset \mathcal{X}$, $T = \{t_j\}_{j=1}^n \subset \mathcal{Y}$ be given point sets. Then, among all the choices of subdividing \mathcal{X} and \mathcal{Y} , $\mathcal{X} = \cup_{i=1}^m Q_i$, and $\mathcal{Y} = \cup_{j=1}^n R_j$, the Voronoi cells $Q_i = V_i$, $R_j = W_j$ minimize a bound on the error term:*

$$\left| \int_{\mathcal{X} \times \mathcal{Y}} c \, d\pi - \int_{\mathcal{X} \times \mathcal{Y}} c \, d\Lambda \right|.$$

Proof.

$$\begin{aligned} \left| \int_{\mathcal{X} \times \mathcal{Y}} c \, d\pi - \int_{\mathcal{X} \times \mathcal{Y}} c \, d\Lambda \right| &\leq \sum_{i=1}^m \sum_{j=1}^n \int_{Q_i \times R_j} |c(x, y) - c(s_i, t_j)| \, d\pi \leq \\ &\sum_{i=1}^m \sum_{j=1}^n \int_{Q_i \times R_j} \lambda [d_{\mathcal{X}}(x, s_i) + d_{\mathcal{Y}}(y, t_j)] \, d\pi = \\ &\lambda \sum_{i=1}^m \int_{Q_i \times \mathcal{Y}} d_{\mathcal{X}}(x, s_i) \, d\pi + \lambda \sum_{j=1}^n \int_{\mathcal{X} \times R_j} d_{\mathcal{Y}}(y, t_j) \, d\pi = \\ &\lambda \sum_{i=1}^m \int_{Q_i} d_{\mathcal{X}}(x, s_i) \, d\nu + \lambda \sum_{j=1}^n \int_{R_j} d_{\mathcal{Y}}(y, t_j) \, d\mu, \end{aligned}$$

and it is not hard to see that the choices of R_i, Q_j that minimizes this last error bound are the Voronoi cells $R_i = V_i$, and $Q_j = W_j$, where $\{V_i\}, \{W_j\}$ are the Voronoi cells corresponding to S, T , respectively. \square

PRINCETON UNIVERSITY